# Reexamining the Estimation of Tropical Cyclone Radius of Maximum Wind from Outer Size with an Extensive Synthetic Aperture Radar Dataset

Arthur Avenas, Alexis Mouche, Pierre Tandeo, Jean-Francois Piolle, Dan Chavas, Ronan Fablet, John Knaff, Bertrand Chapron

# Reexamining the Estimation of Tropical Cyclones Radius of Maximum Wind from Outer Size with an Extensive Synthetic Aperture Radar Dataset

Arthur Avenas,[a, b] Alexis Mouche,[a] Pierre Tandeo,[b] Jean-Francois Piolle,[a] Dan Chavas,[c] Ronan Fablet,[b] John Knaff,[d] Bertrand Chapron,[a]

[a] *Ifremer, Univ. Brest, CNRS, IRD, Laboratoire d'Océanographie Physique et Spatiale (LOPS), IUEM, F-29280, Plouzané, France*

[b] *IMT Atlantique, Lab-STICC, Université Bretagne Loire, Brest, France*

[c] *Purdue University, Department of Earth, Atmospheric, and Planetary Sciences, West Lafayette, Indiana*

[d] *NOAA/NESDIS Regional and Mesoscale Meteorological Branch, Fort Collins, Colorado*

*Corresponding author*: Arthur Avenas, arthur.avenas@ifremer.fr

ABSTRACT: The radius of maximum wind ($R_{max}$), an important parameter in tropical cyclones (TCs) ocean surface wind structure, is currently resolved by only a few sensors, so that, in most cases, it is estimated subjectively or via crude statistical models. Recently, a semi-empirical model relying on an outer wind radius, intensity and latitude was fit to best-track data. In this study we revise this semi-empirical model and discuss its physical basis. While intensity and latitude are taken from best-track data, $R_{max}$ observations from high-resolution (3 $km$) spaceborne synthetic aperture radar (SAR) and wind radii from an inter-calibrated dataset of medium-resolution radiometers and scatterometers are considered to revise the model coefficients. The new version of the model is then applied to the period 2010-2020 and yields $R_{max}$ reanalyses and trends more accurate than best-track data. SAR measurements corroborate that fundamental conservation principles constrain the radial wind structure on average, endorsing the physical basis of the model. Observations highlight that departures from the average conservation situation are mainly explained by wind profile shape variations, confirming the model's physical basis, which further shows that radial inflow, boundary layer depth and drag coefficient also play roles. Physical understanding will benefit from improved observations of the near-core region from accumulated SAR observations and future missions. In the meantime, the revised model offers an efficient tool to provide guidance on $R_{max}$ when a radiometer or scatterometer observation is available, for either operations or reanalysis purposes.

## 1. Introduction

Estimating tropical cyclone (TC) ocean surface wind structure is challenging but crucial for several applications. In particular, TC surface wind spatio-temporal distributions are used as input of surface wave studies (Wright et al. 2001; Young 2017; Kudryavtsev et al. 2021), storm surge studies (Irish et al. 2008; Takagi and Wu 2016), or the upper ocean responses to TC passages (Price 1981; Ginis 2002; Kudryavtsev et al. 2019; Combot et al. 2020b). In such studies, the radius of maximum winds (hereafter $R_{max}$) is a critical parameter that significantly affects the wave developments, surges estimates, sea surface height, temperature and salinity variations within the TC wakes. Most parametric surface wind fields, often used for those applications, assume that $R_{max}$ is known (Holland 1980; Willoughby et al. 2006). Thus, $R_{max}$ errors cascade into errors for the entire spatial distribution of wind speeds. Figure 1 shows a comparison between two Rankine profiles for two different $R_{max}$ values

$$V_{Rankine}(r) = \begin{cases} V_{min} + (V_{max} - V_{min})(\frac{r}{R_{max}}) & \text{if } r \leq R_{max} \\ V_{min} + (V_{max} - V_{min})(\frac{R_{max}}{r}) & \text{if } r > R_{max} \end{cases} \quad (1)$$

TC Lane, a North Eastern Pacific hurricane that reached category 5 on the Saffir-Simpson scale in 2018, provides an example of such a situation. TC Lane's wind speeds were estimated by a swath of satellite-based SAR observation on 23 August at 0437 UTC. From the SAR wind speeds, the azimuthally-averaged wind profile can be derived (dashed green curve in Fig. 1). The inferred $R_{max}$ is 15 $km$, about 2 to 3 times smaller than the 37 $km$ value interpolated to the SAR aquisition time in the best-track data (Knapp et al. (2010); hereafter IBTrACS). Such a mismatch between best-track and SAR $R_{max}$ estimates is representative of what has been reported in the literature (Combot et al. 2020a). In the present case (Fig. 1), this discrepancy results into a Mean Absolute Error (MAE) as high as 28 $ms^{-1}$ near the eyewall region when using subsequent Rankine profile estimates.

To date, airborne Stepped Frequency Microwave Radiometer (SFMR) surface winds (Uhlhorn et al. 2007) provide means to estimate $R_{max}$. Yet, airborne measurements have limited azimuthal coverage, and are operated over only few ocean regions and events. From a satellite perspective, high spatial resolution estimates of TC ocean surface wind field are now more systematically carried out, especially from SAR dedicated acquisitions (Mouche et al. 2017; Combot et al. 2020a). More

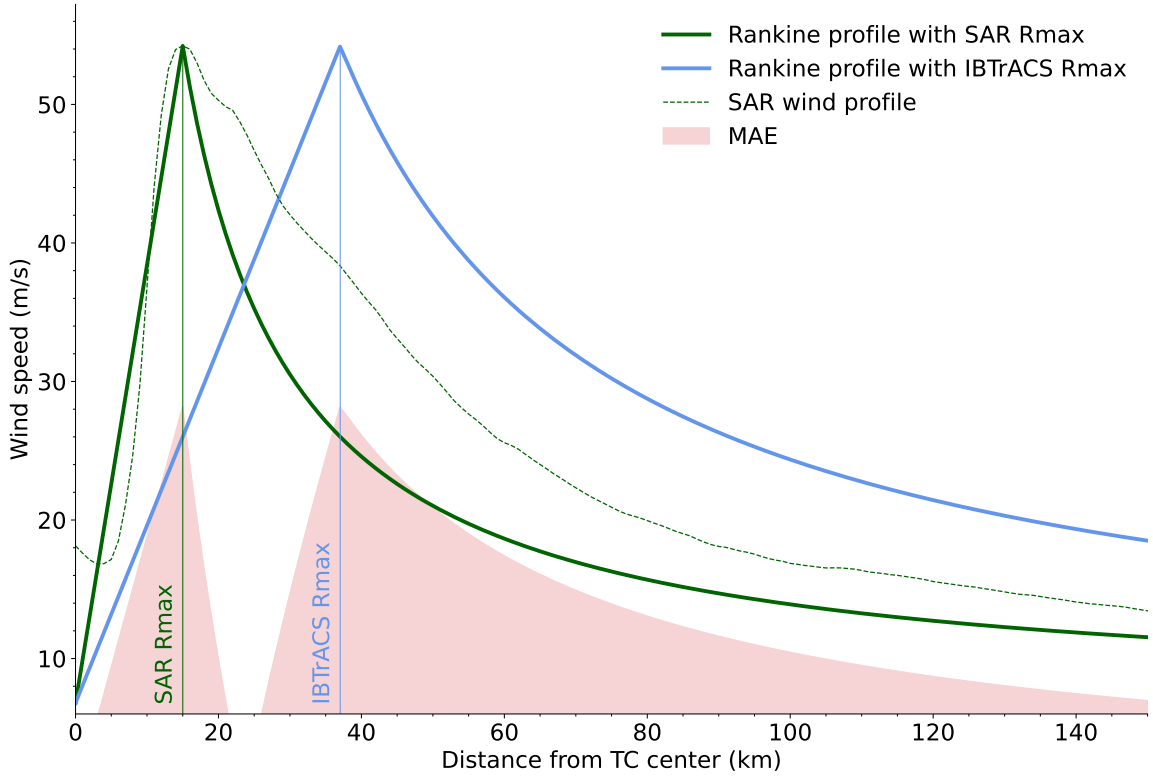


FIG. 1. Comparison between two Rankine profiles inspired by the SAR acquisition over TC Lane on 23 August 2018 at 0437 UTC. Rankine profiles are defined with SAR $R_{max}$ (15 $km$, solid green) or IBTrACS $R_{max}$ (37 $km$, solid blue) and the same $V_{max}$ (54 $ms^{-1}$) and $V_{min}$ (7 $ms^{-1}$), consistently with the SAR azimuthally-averaged profile (dashed green). MAE between the two Rankine profiles is shaded in red.

reliable $R_{max}$ estimates are then obtained for all ocean basins, though with limited spatio-temporal sampling. Presently, the most often available spaceborne observing systems, capable of probing the ocean surface during TC conditions, are the combined capabilities from active scatterometers and passive radiometers (Quilfen et al. 2007). Compared to radiometers, scatterometers generally have an improved medium spatial resolution. Yet, the strong gradients of the surface wind existing at scales of a few kilometers may still be smoothed to precisely locate the wind maxima, and the position of the center (Quilfen et al. 1998). In addition, scatterometers, especially those operating at Ku-band and higher microwave frequencies, can suffer from rain contamination. Signal sensitivity at high winds, above hurricane force wind (33 $ms^{-1}$), has also been questioned (Donnelly et al. 1999; Mouche et al. 2019). Radiometer measurements may be less impacted by rain, especially those operating at L-band (Reul et al. 2012, 2017), and demonstrated to be still highly sensitive

above hurricane force winds. However, actual spaceborne radiometers operating at L- or C-band have a lower spatial resolution. High wind speed gradients near the $R_{max}$ region for most intense TCs are then generally indistinct. Direct estimates of $R_{max}$ using scatterometers or radiometers are thus difficult to perform, possibly limited to particular large storm cases.

More indirect means to infer $R_{max}$ were also considered. Both Mueller et al. (2006) and Kossin et al. (2007) used geostationary infrared satellite data. For the cases where a clear eye is well-defined on the infrared image, using linear regression to estimate $R_{max}$ results in a MAE of only ~5 $km$ when compared to aircraft-based estimates. Under less favourable conditions, $R_{max}$ can still be estimated via multiple linear regression in combination with a principal components analysis, but leads to a degraded MAE of ~20 $km$. Notably, for the clear-eye case, Tsukada and Horinouchi (2023) trained the linear regression with available SAR $R_{max}$ estimates and improved the method, decreasing the MAE to ~2 $km$.

In the absence of infrared data, a rough $R_{max}$ estimate can also be obtained, considering the storm intensity and latitude known, as evidenced by Willoughby et al. (2006) and Vickery and Wadhera (2008). Indeed, following the angular momentum conservation, $R_{max}$ must decrease when the intensity increases. On average, such a physical constrain agrees well with observations (see for instance Fig. 9 in Combot et al. (2020a)). In addition, it is also known that $R_{max}$ increases with latitude (e.g. Willoughby and Rahn (2004)), another consequence of angular momentum conservation along with the decrease of intensity with latitude. Solely using intensity and latitude to predict $R_{max}$ yields a root-mean square error of the order ~20 $km$. Results from Vickery and Wadhera (2008) show that in several cases, the observed $R_{max}$ is inconsistent with the general principle of angular momentum conservation. This suggests that $R_{max}$ natural variability can hardly be captured by such simple statistical models.

More recently, Chavas and Knaff (2022) - hereafter CK22 - suggested to use information on the TC outer-size in combination with latitude and intensity. In CK22 framework, $R_{max}$ is estimated from the TC intensity $V_{max}$, the radius of gale $R_{34}$ (*i.e* the maximum radial extent of the 34-knots winds) and the Coriolis parameter, defined as $f = 2\Omega sin(\phi)$, where $\Omega = 7.292x10^{-5}\ s^{-1}$ is the Earth angular velocity and $\phi$ is the latitude of the TC center. Such an approach is practical, especially because $R_{34}$ is well estimated by satellite scatterometers and radiometers (Brennan et al. 2009;

Chou et al. 2013; Reul et al. 2017). In fact, $R_{34}$ estimates are routinely produced for every TC and included in IBTrACS.

The CK22 framework is based on physical understanding of the radial wind structure (Emanuel 2004; Emanuel and Rotunno 2011) and phrased in terms of absolute angular momentum $M(r) = rV + \frac{1}{2}fr^2$, where $f$, $r$ and $V$ are the Coriolis parameter, the radius and the tangential wind speed of an air parcel, respectively. If the ratio $\frac{M_{max}}{M_{34}} := \frac{M(r=R_{max})}{M(r=R_{34})}$ is prescribed, one can then estimate $R_{max}$ provided estimates for the 3 above-mentioned parameters using:

$$R_{max} = \frac{V_{max}}{f}\left(\sqrt{1 + \frac{2fM_{max}}{V_{max}^2}} - 1\right) \tag{2}$$

CK22 fitted a log-linear regression model to estimate the ratio $\frac{M_{max}}{M_{34}}$ with the two predictors $X_{34}^{(1)} := (V_{max} - 17.5ms^{-1})$ and $X_{34}^{(2)} := (V_{max} - 17.5ms^{-1})(\frac{1}{2}fR_{34})$.

It is tempting to use this framework in combination with best-track data. CK22 used best-track estimates (in a region west of 50°W) of $R_{max}$, $V_{max}$, $R_{34}$ and latitude to fit the log-linear regression model. As a result, their model inherited best-track biases. In particular, the reported $R_{max}$ overestimation in best-tracks compared to SAR (Combot et al. 2020a) translated into an overestimation of the ratio $\frac{M_{max}}{M_{34}}$ during the regression training, further leading to overestimated $R_{max}$ values.

The quality of $R_{34}$ best-track estimates has also already been questioned (Sampson et al. 2017). This parameter is reanalyzed and compiled in IBTrACS since 2004 for North Atlantic and North Eastern Pacific and since 2016 for North Western Pacific (Knaff et al. 2021). Yet, surveying specialists who produce best-tracks in the Atlantic ocean (Landsea and Franklin 2013) are on average much less confident in their wind radii estimates (~25-50% of relative uncertainty) than in their intensity estimates (~10-20%).

In addition, best-tracks may also suffer from temporal and spatial heterogeneities (Schreck III et al. 2014; Wang and Toumi 2021). Indeed, the reanalysis methodology depends on the available data at each reanalysis time: best-track estimates of TC events covered by aircraft data are for instance more trustworthy (Landsea and Franklin 2013). Reanalysis is also subjective, each agency or Regional Specialized Meteorological Center (RSMC) specialist conducting his own weighting of

the available observations. Lastly, best-tracks are finalized annually and not updated with evolving reanalysis methodology, creating a temporal discontinuity in the final IBTrACS database.

Finally, a possible limitation of the CK22 approach is the arbitrary choice of the outer wind radius $R_{34}$. Indeed, their model could well be trained using $R_{50}$ or $R_{64}$. In CK22, the choice of $R_{34}$ was motivated by the fact that best-track estimates of $R_{50}$ and $R_{64}$ are generally more uncertain than $R_{34}$ estimates. With more reliable $R_{50}$ and $R_{64}$ estimates, possibly obtained from radiometer or scatterometer observations, one could assess whether using these wind radii would improve the CK22 model.

The physical basis for wind structure relationships such as CK22 is a long-running issue. The assumption that an outer wind radius partly constrains the wind structure dates back to Riehl (1963). Riehl (1963) used a two-layer conceptual model constrained by an angular momentum conservation in the outflow and a potential vorticity (PV) conservation in the inflow layer. Riehl (1963) could then derive a relationship between $R_{max}$, $V_{max}$, $f$, and an outer radius $R_{out}$, corresponding to a distance where the outflow velocity vanishes. Later, Kalashnik (1994) considered the Holland parametric profile (Holland 1980) within a theoretical framework, to analyze the dependence of the near-core wind structure on the wind profile. Emanuel and Rotunno (2011) also derived an analytical solution for the near-core wind profile based on an assumption on the outflow temperature.

While these studies offer theoretical guidance, these theoretical inferences of $R_{max}$ are difficult to apply in practice. Indeed, most actual sensors fail to capture the wind profile shape used in Kalashnik (1994), while the model of Emanuel and Rotunno (2011) relies on parameters that are difficult to evaluate. Following Riehl (1963), the theoretical outer radius $R_{out}$ is unknown and cannot be specified to correspond to a given surface wind speed.

Building on the above considerations, the aim of this study is twofold. First, the CK22 model is revised using SAR $R_{max}$ estimates, different wind radii (referring hereafter to $R_{34}$, $R_{50}$, and $R_{64}$) estimated on inter-calibrated radiometers and scatterometers, and intensity and latitude best-track estimates. Second, the physical basis of the CK22 model is further assessed through an examination of conservation equations and a thorough analysis of the SAR database.

The data used in the present work are introduced in section 2 and further analysed in section 3. Then, the CK22 model is revised and its performance assessed in section 4. Finally, the physical

basis of the model is discussed with respect to SAR observations in section 5. Concluding remarks and possible routes for future investigations are provided in the last section.

## 2. Data

In the present work, different radiometer and scatterometer data (table 1) over the period 2010-2020 were used to estimate wind radii ($R_{34}$, $R_{50}$, and $R_{64}$), while SAR data (table 2) were used to estimate the $R_{max}$ values required to fit the CK22 log-linear model. Furthermore, IBTrACS provided intensity and latitude estimates ($V_{max}$ and $f$).

We used different radiometer and scatterometer missions to constitute the most extensive dataset of $R_{max}$ reanalyses. These sensors rely on different physical principles (passive or active sensors), and have different frequencies (L-band, C-band or Ku-band) and spatial resolutions. In order to ensure homogeneity of the wind radii estimates, we used radiometer and scatterometer winds inter-calibrated by Portabella et al. (2022).

A thorough analysis of this database revealed that the wind profiles issued from Ku-band scatterometer data barely exceed 64 knots, even for most intense TCs, as shown in appendix A. Thus, we chose to remove Ku-band scatterometers from the present analysis.

### *a. Radiometer missions*

Because both the foam coverage and bubble surface layer thickness increase with surface wind speed (Reul and Chapron 2003), passive microwave measurements have long been known to display very high sensitivity under extreme wind conditions. With large $\sim$1000 $km$ swaths, satellite-borne radiometers are well suited to monitor TCs. However, they have nominally low spatial resolutions ($\sim$40 $km$) that generally prevent accurate retrieval of the extreme surface wind speeds associated with the inner-core of most intense TCs. The radiometer wind products used in this work are at 50 $km$ spatial resolution with a 25 $km$ grid spacing (Portabella et al. 2022).

In the present study, four different sources of radiometer data were used. Among them, the L-band (1.4 GHz, 21 cm wavelength) radiometers from the European Space Agency (ESA) Soil Moisture and Ocean Salinity (hereafter SMOS) mission and the National Aeronautics and Space Administration (NASA) Soil Moisture Active Passive (hereafter SMAP). The ability of L-band radiometers to retrieve ocean surface wind speeds under TCs has been discussed both in the case

of SMOS (Reul et al. 2012, 2016) and SMAP (Yueh et al. 2016; Meissner et al. 2017). Reul et al. (2017) demonstrated that SMOS, SMAP, as well as AMSR-2 can be used to estimate wind radii.

The Japan Aerospace Exploration Agency launched the Advanced Microwave Scanning Radiometer 2 (hereafter AMSR-2) onboard the Global Change Observation Mission Water 1 satellite in 2012. This instrument is still operating today and uses 7 different frequencies (6.93, 7.3, 10.65, 18.7, 23.8, 36.5 and 89.0 GHz. For TCs, the first 3 channels (6.93, 7.3, and 10.65 GHz) are used. With two C-band channels, initially intended for radio-frequency interference identification, surface wind estimates are improved. Signals at these two C-band frequencies have similar sensitivity to the sea wind speed but differ in sensitivity to rain by about 12%. Accuracy of the AMSR-2-retrieved wind speed in storms is comparable to results obtained from SMOS and SMAP L-band sensors (Zabolotskikh et al. 2015; Reul et al. 2017).

Windsat is a polarimetric radiometer onboard Coriolis, a mission designed by the Naval Research Laboratory and the Air Force Research Laboratory, and launched in 2003. The sensor provided data until May 2021. This instrument operates at 5 different channels (6.8, 10.7, 18.7, 23.8 and 37.0 GHz). To minimize heavy precipitation impacts, the C-band 6.8 and the X-band 10.7 GHz channels are used for TC wind retrieval algorithms. Again, changes in the respective contribution of wind and rain to the signal measured by each channel can be used to better infer and discriminate both quantities (Klotz and Uhlhorn 2014). Heavy precipitation is still found to complicate surface wind speed retrieval with this sensor (Quilfen et al. 2007), and more recent studies addressed this issue (Meissner et al. 2021; Manaster et al. 2021).

*b. Scatterometer missions*

Scatterometers are active sensors that emit a pulse and measure the signal backscattered by the rough ocean surface with different viewing angles. Because backscatter signals are dependent upon both wind speed and wind direction, ocean surface wind vectors can be retrieved. The achieved nominal spatial resolution (up to ~25 $km$) is higher than satellite-borne radiometers. Actual scatterometers operate at different frequencies (C-band or Ku-band).

The Meteorological Operational satellite programme is a series of 3 satellites (Metop-A, -B and -C) launched by ESA (in 2006, 2012 and 2018, respectively) which include scatterometers (ASCAT, for "Advanced Scatterometer") operating at 5.3 GHz (C-band). With 3 antennas oriented

at 45°, 90° and 135° with respect to the satellite track, the wind direction can be retrieved. ASCAT instruments have 2 sub-swaths, each having a width of ~550 $km$. At C-band, the signal may be influenced by very heavy rain. Backscatter signals also tend to saturate at high winds (Donnelly et al. 1999), and ASCAT measurements progressively lose sensitivity under high wind speeds (Soisuvarn et al. 2012; Polverari et al. 2021). The ASCAT wind product used in the present study is at 25 $km$ spatial resolution with a 12.5 $km$ grid spacing (Stoffelen et al. 2017; Portabella et al. 2022).

Scatterometers operating at Ku-band (~ 13.5 GHz) usually have larger swaths (~1000 $km$) than C-band scatterometers, but suffer more contamination in heavy rainfall conditions (see Quilfen et al. (2007) for more details). The Ku-band scatterometer wind products used in Portabella et al. (2022) were finally removed (see appendix A). They include the China National Space Administration (CNSA) Haiyang missions (hereafter HSCAT), the Indian Space Research Organisation (ISRO) OceanSat-2 and SCATSat-1 satellites (hereafter OSCAT), and the NASA RapidScat (hereafter RSCAT) onboard the International Space Station (Table 1).

| **RADIOMETER** | SMOS | SMAP | AMSR-2 | Windsat |
|---|---|---|---|---|
| Period | 2010-2020 | 2015-2020 | 2012-2020 | 2010-2019 |
| Spatial resolution | 50 $km$ | 50 $km$ | 50 $km$ | 50 $km$ |
| Pixel spacing | 25 $km$ | 25 $km$ | 25 $km$ | 25 $km$ |
| Frequency | L-band | L-band | C-band, X-band | C-band, X-band |
| **SCATTEROMETER** | ASCAT | HSCAT | OSCAT | RSCAT |
| Period | 2010-2020 (Metop-A) | 2012-2015 (HY-2A) | 2010-2014 (Oceansat-2) | 2014-2016 |
| | 2012-2020 (Metop-B) | 2019-2020 (HY-2B) | 2017-2020 (Scatsat-1) | |
| | 2019-2020 (Metop-C) | | | |
| Spatial resolution | 25 $km$ | 50 $km$ | 50 $km$ | 50 $km$ |
| Pixel spacing | 12.5 $km$ | 25 $km$ | 25 $km$ | 25 $km$ |
| Frequency | C-band | Ku-band | Ku-band | Ku-band |

TABLE 1. The radiometer and scatterometer data used in Portabella et al. (2022). The period, spatial resolution, and pixel spacing rows refer to the wind product. The same data were used for the present work, except the Ku-band scatterometers, which were removed from the analysis.

### c. SAR missions

The SAR data used here come from three different missions: ESA Sentinel-1A and Sentinel-1B (hereafter S1A and S1B, respectively), and the Canadian Space Agency (CSA) Radarsat-2 (hereafter RS2). The SAR instrument onboard these three missions is an active sensor operating at 5.4 GHz (C-band). By analysing the received signal in both co- and cross-polarization, wind speeds can be inferred under TC conditions including at very high wind speeds (Mouche et al. 2017, 2019). Convincing comparisons with passive radiometers have been performed (Zhao et al. 2018). The ability of SAR-derived wind speeds to accurately capture the TC ocean surface wind structure, including $R_{max}$, has further been demonstrated and discussed by Combot et al. (2020a).

Today, SAR wide-swath acquisitions cannot be continuously performed over oceans. Based on track forecasts, it is still possible to best anticipate when the sensor will overpass a TC, and to trigger a SAR acquisition. ESA started the Satellite Hurricane Observation Campaign (SHOC) in 2016, resulting in more than ~500 acquisitions over TCs. The derived wind products (Mouche et al. 2017) are further interpolated on a regular polar grid based on the TC center (see appendix in Vinour et al. (2021)). The product has a 3 $km$ spatial resolution, with a 1 $km$ grid spacing. This spatial resolution approximates a 1-minute wind speed as a 50 $ms^{-1}$ wind moves 3 $km$ in a minute. In this study, a certain number of SAR cases have been discarded on a qualitative basis, e.g. when the detected TC center was judged to be wrong, or when the SAR file contained corrupted pixel values.

| **SAR** | S1A | S1B | RS2 |
|---|---|---|---|
| Period | 2016-2021 | 2016-2021 | 2012-2021 |
| Spatial resolution | 3 $km$ | 3 $km$ | 3 $km$ |
| Pixel spacing | 1 $km$ | 1 $km$ | 1 $km$ |
| Frequency | C-band | C-band | C-band |

TABLE 2. The SAR data used in the present study. The period, spatial resolution, and pixel spacing rows refer to the wind product.

### d. Best-tracks

Here, IBTrACS were used for several purposes: the storm centers (latitude and longitude) allowed to azimuthally average the radiometer and scatterometer wind fields, while the wind radii ($R_{34}$,

$R_{50}$, and $R_{64}$) were compared to satellite-based wind radii. Both IBTrACS latitude (to compute $f$) and maximum sustained wind speed ($V_{max}$) were used in the CK22 framework, and the distance to closest land (from the TC center) enabled filtering of the dataset. These parameters were extracted for the period 2010-2020.

In IBTrACS, some storm tracks are given on a six-hourly basis, while others are interpolated and thus given on a three-hourly basis. To account for this varying sampling time, all tracks and their associated parameters were interpolated to an hourly basis with a monotonic cubic interpolation. Lastly, because of varying definitions of the maximum sustained wind speed across the different agencies, we selected only USA agencies (*i.e* National Hurricane Center, Joint Typhoon Warning Center, and Central Pacific Hurricane Center) which all provide the 1-minute maximum sustained wind speed.

### *e. Data filtering*

To further restrain the analysis to well-formed systems, i.e. for which $R_{max}$ can be well determined from the axisymmetric mean profile, and to best ensure consistency with CK22 for further comparison, the following filters have been applied to our dataset:

1. $V_{max} > 20\ ms^{-1}$;
2. $R_{max} < 150\ km$;
3. Any wind radius must be $> 5\ km$;
4. Absolute latitude $< 30°$;
5. Distance to closest land $> R_{34}$.

Unlike CK22, we didn't apply any filter on longitude. Therefore, the method presented here applies in every basin and does not depend on the availability of aircraft analysis.

## 3. Methods and data analysis

### *a. Estimation of the CK22 predictors*

In order to apply the CK22 framework to the inter-calibrated dataset of radiometer and scatterometer data, estimates of the predictors ($V_{max}$, $R_{34}$, $f$) were needed for every satellite file.

Regarding the wind radii, an azimuthally-averaged wind profile was first computed for every satellite file using the corresponding IBTrACS center linearly-interpolated to the acquisition time. For each of the three speed values of interest (*i.e* 34, 50 and 64 knots), we then selected the radius where the outer-profile matches this value to the closest kilometer. Should there be more than one radius value, the wind radius was defined as the smallest of the radii.

Unlike the wind radii, $V_{max}$ and $f$ cannot be accurately estimated from radiometer and scatterometer data, especially for intense small TCs, but both parameters are systematically reanalyzed in the best-tracks. However, IBTrACS $V_{max}$ definition does not strictly coincide with the axi-symmetric view adopted here. In particular, the analysis (appendix A) highlighted that $V_{max}$ estimated using SAR azimuthally-averaged profiles were, on average, lower than IBTrACS $V_{max}$. This can be modeled by applying a linear regression (dashed grey line in Fig. A1) to IBTrACS $V_{max}$ estimates. The resulting intensity estimates are denoted by $V_{max}^{REG}$ and were used (instead of the raw IBTrACS $V_{max}$) to ensure the consistency with the wind radii defined on azimuthally-averaged wind profiles. The pair of parameters ($V_{max}^{REG}$, $f$) was then linearly-interpolated to the satellite acquisition time for every file.

*b. Quality assessment of radiometer and scatterometer wind radii estimates*

To assess the quality of the satellite-based wind radii, comparisons were performed with IBTrACS wind radii. A strict comparison cannot be achieved because of varying definitions. In IBTrACS, wind radii are relative to the geographical quadrants and correspond to the maximum radial extent of the associated wind speed in each of the four quadrants. To make IBTrACS values as close as possible to the satellite-based wind radii, the nonzero IBTrACS values were averaged over all the quadrants. Furthermore, both the methodologies and the available observational data can vary across the IBTrACS dataset. Here, the adopted strategy was to compare the whole IBTrACS wind radii dataset (including non-USA agencies for this section) to the satellite-based wind radii. Accounting for the differences between the specialists and agencies is beyond the scope of this study. Finally, after removing the Ku-band sensors (see appendix A), we separated radiometer wind radii from the C-band scatterometer wind radii to further investigate possible discrepancies between the remaining sensors.

Figure 2 shows a comparison between radiometer wind radii and IBTrACS values (top) and their corresponding distributions (bottom). While radiometer wind radii look well correlated with IBTrACS values, with $R^2$-scores ranging from 0.4 to 0.5, large discrepancies arise, with a Residual Standard Deviation (RSD) as high as 56.7 $km$ for $R_{34}$. The RSD decreases to 37.3 $km$ for $R_{50}$, and further to 24.1 $km$ for $R_{64}$, reflecting the decrease of the mean wind radius, i.e. 181 $km$ for $R_{34}$ to 51 $km$ for $R_{64}$ in IBTrACS. In terms of relative uncertainties, this leads to ~31%, ~36%, and ~41% for $R_{34}$, $R_{50}$, and $R_{64}$, respectively. Interestingly, the Mean Error (ME) is negative for both $R_{34}$ and $R_{50}$, showing that, on average, these wind radii are lower when extracted from azimuthally-averaged radiometer profiles than from IBTrACS. This is likely the result of the differing definition of the wind radii in the satellite data and in IBTrACS. Indeed, on average, a wind radius extracted from an azimuthally-averaged profile is expected to be smaller than the maximum radial extent of the same wind speed. Biases due to the differing definition are lower for $R_{50}$ and $R_{64}$ than for $R_{34}$, because these radii are smaller on average. This definition effect is illustrated on the distribution for $R_{34}$, where the radiometer $R_{34}$ distribution is biased toward lower values compared to IBTrACS.

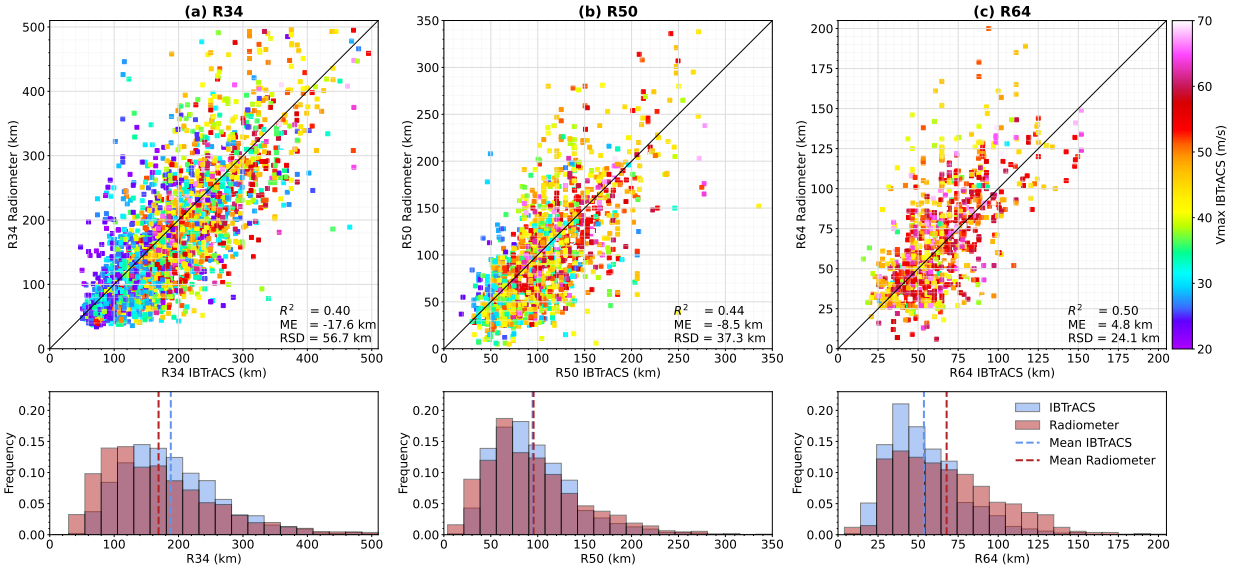


FIG. 2. (Top) Comparison between radiometer (y-axis) and corresponding IBTrACS (x-axis) wind radii. Coefficient of determination ($R^2$), Mean Error (ME) and Residual Standard Deviation (RSD) are displayed. (Bottom) Corresponding distributions and averages.

Figure 3 shows comparisons between C-band scatterometer wind radii and IBTrACS values. Again, an overall consistency emerges between both data sources for all wind radii. RSD values

and $R^2$ scores are comparable to the previous comparisons between radiometer and IBTrACS. Data and methodology are thus consistent with IBTrACS (which is expected since radiometer and scatterometer data are often used during the reanalysis process), but it also shows that there is a good consistency between the various sensors in terms of wind radii.

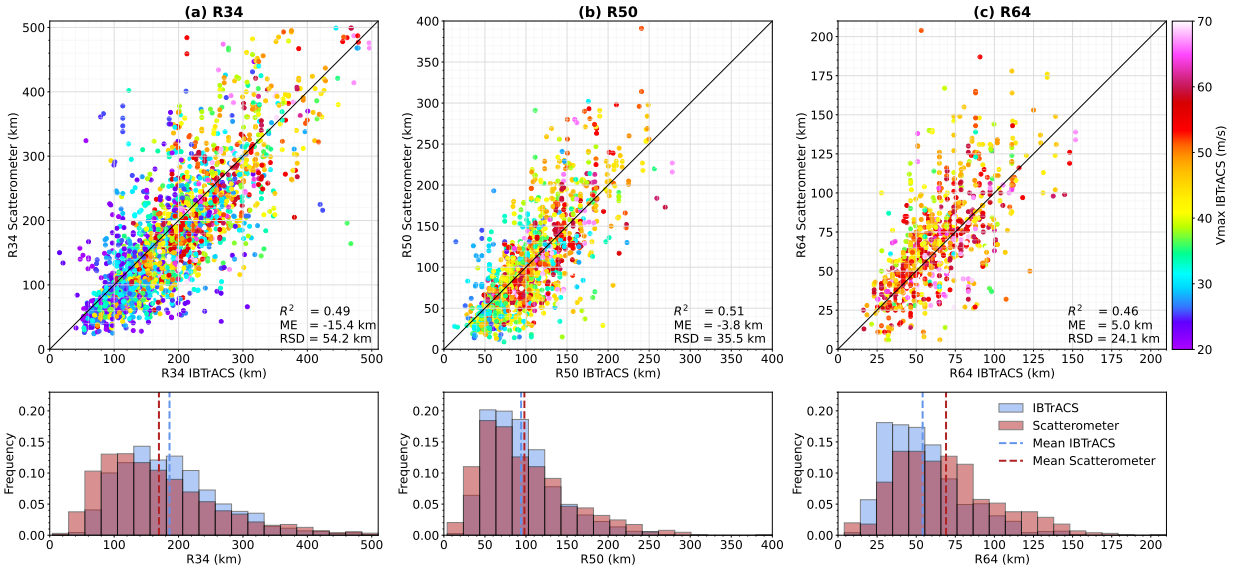


FIG. 3. Same as Fig. 2, but for the C-band scatterometer wind radii.

Regarding $R_{64}$, the ME is slightly positive for both radiometer and scatterometer data (Figs. 2c and 3c), with a distribution of $R_{64}$ skewed toward higher values for the satellite data compared to IBTrACS. First, this could be attributed to the satellite data limitations, such as low spatial resolution, signal saturation or rain contamination. Yet, Fig. 4 offers a different explanation. It again shows comparisons between scatterometer wind radii and IBTrACS values, but only over the 3-year period from 2018 to 2020. For such a period, the computed ME for $R_{64}$ is only 1.5 $km$ (Fig. 4c), and the RSD drops to 19.4 $km$ (compared to 24.1 $km$ for the period 2010 to 2020). Consistency between scatterometer and IBTrACS also improves for both $R_{34}$ and $R_{50}$ over the same period (Figs. 4a and 4b). The positive ME for $R_{64}$ in Fig. 3 likely corresponds to the improving quality of IBTrACS over the years. Mentioned in the introduction, wind radii best-track values were not necessarily reanalyzed depending on the year and the basin. Similar conclusions were obtained with radiometer data (not shown).

To summarize, the comparison between IBTrACS and the inter-calibrated dataset shows that radiometers and scatterometers provide reliable wind radii estimates. Thus, for every radiometer

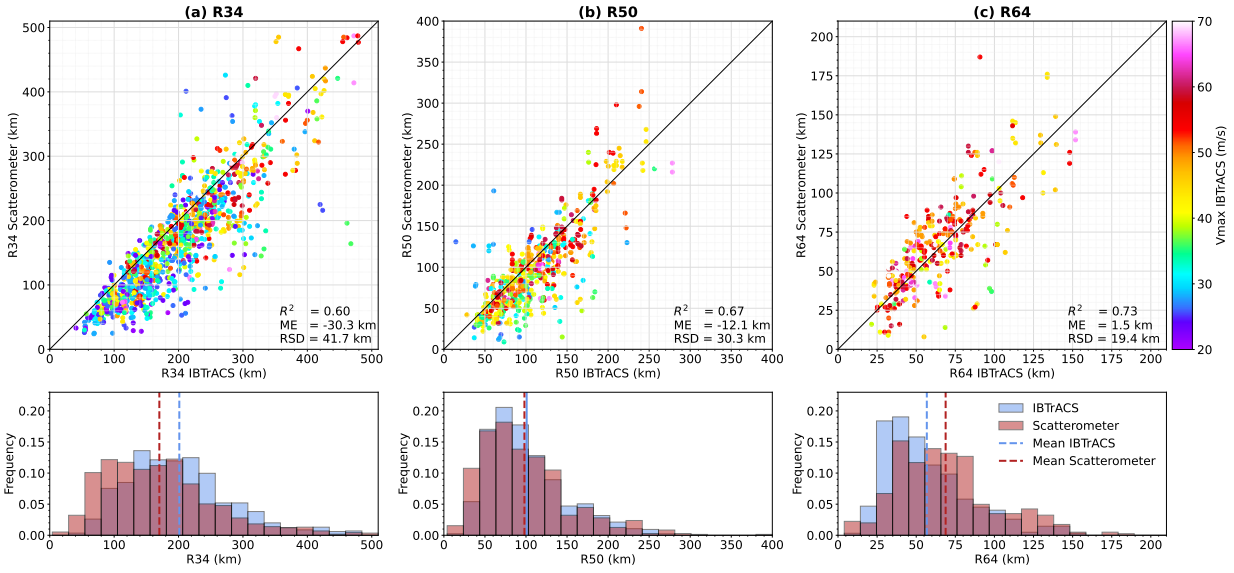


FIG. 4. Same as Fig. 3, but only for the 3-year period 2018-2020.

or scatterometer acquisition, we can extract a corresponding set of predictors constituted by a satellite-based wind radius along with IBTrACS $V_{max}^{REG}$ and $f$ estimates.

### *c. Collocations of radiometers and scatterometers with SAR*

In order to fit the CK22 model, we also needed an estimate of the predictand ($R_{max}$) for each set of predictors. The latter cannot be directly evaluated from radiometer and scatterometer data, but is well observed on SAR data by taking the location of the wind profile maximum. Thus, we looked for collocations between SAR and radiometer or scatterometer TC overpasses. Two images were considered to be collocated if their absolute acquisition time difference is less than 90 minutes.

Regarding radiometer data (table 3, first four columns), this procedure resulted in a total of 269 collocations, which further reduced to 145 collocations after applying filters presented in section 3e. Notably, no collocation was found between any of the 3 SAR missions (S1A, S1B, RS2) and AMSR-2.

Regarding scatterometer data, no collocation was found between SAR and ASCAT (Table 3, penultimate column). In what follows, we thus refers to the dataset obtained by this collocation procedure as the "SAR-radiometer collocation dataset". It consists in predictors estimated on radiometer data (wind radii) or corresponding IBTrACS values ($V_{max}^{REG}$ and $f$), and predictands estimated on SAR ($R_{max}$).

| | SMOS | SMAP | AMSR-2 | Windsat | ASCAT | TOTAL |
|---|---|---|---|---|---|---|
| Before filtering | 106 | 63 | 0 | 100 | 0 | 269 |
| After filtering | 67 | 33 | 0 | 45 | 0 | 145 |

TABLE 3. Number of collocations between SAR and the inter-calibrated dataset (radiometer and ASCAT).

## 4. Results

### *a. Fitting CK22 model*

As explained in the introduction, the CK22 model relies on the estimation of the ratio $\frac{M_{max}}{M_{34}}$ via a log-linear regression model, using $(X_{34}^{(1)}, X_{34}^{(2)})$ as input. While CK22 used $R_{34}$ in their study, this method is in fact agnostic from the choice of wind radius. Therefore, the ratio $\frac{M_{max}}{M_{50}}$ can also be estimated using $X_{50}^{(1)} := V_{max} - 25.7ms^{-1}$ and $X_{50}^{(2)} := (V_{max} - 25.7ms^{-1})(\frac{1}{2}fR_{50})$ as input (or $\frac{M_{max}}{M_{64}}$ using $X_{64}^{(1)} := V_{max} - 32.9ms^{-1}$ and $X_{64}^{(2)} := (V_{max} - 32.9ms^{-1})(\frac{1}{2}fR_{64})$ as input).

CK22 estimated the coefficients of the log-linear regression model based solely on IBTrACS rather than direct observational estimates, and only for the ratio $\frac{M_{max}}{M_{34}}$. In the present work, we use observational data not only to obtain improved estimates of the predictors in the CK22 model framework, but also to obtain improved estimates of the model coefficients that relate the parameters to one another. We also extend the CK22 model for the ratios $\frac{M_{max}}{M_{50}}$ and $\frac{M_{max}}{M_{64}}$. A log-linear regression model was fitted for each of the three ratios using the SAR-radiometer collocation dataset previously presented. The following relationships were obtained:

$$\frac{M_{max}}{M_{34}} = 0.531e^{-0.00214(V_{max}^{REG} - 17.5ms^{-1}) - 0.00314(V_{max}^{REG} - 17.5ms^{-1})(\frac{1}{2}fR_{34})} \tag{3}$$

$$\frac{M_{max}}{M_{50}} = 0.626e^{0.00282(V_{max}^{REG} - 25.7ms^{-1}) - 0.00724(V_{max}^{REG} - 25.7ms^{-1})(\frac{1}{2}fR_{50})} \tag{4}$$

$$\frac{M_{max}}{M_{64}} = 0.612e^{0.00946(V_{max}^{REG} - 32.9ms^{-1}) - 0.01183(V_{max}^{REG} - 32.9ms^{-1})(\frac{1}{2}fR_{64})} \tag{5}$$

With these formulas, $R_{max}$ can then be estimated using the steps presented in the introduction (eq. 2). Subsequent estimates will be referred to as $R_{max}^{CK22-R_{34}}$, $R_{max}^{CK22-R_{50}}$, or $R_{max}^{CK22-R_{64}}$ depending on which wind radius is used.

*b. Assessment of the resulting $R_{max}$ estimates*

To check the fitting procedure, we compared $R_{max}^{CK22-R_{34}}$ estimates and SAR $R_{max}$ (Fig. 5a). The consistency between both is reasonably good, with a $R^2$-score of 0.41 and a RSD of 10.6 $km$. A low ME of 3.7 $km$ is observed, which can be related to the distribution of $R_{max}^{CK22-R_{34}}$ being slightly skewed toward higher $R_{max}$ values compared to SAR.

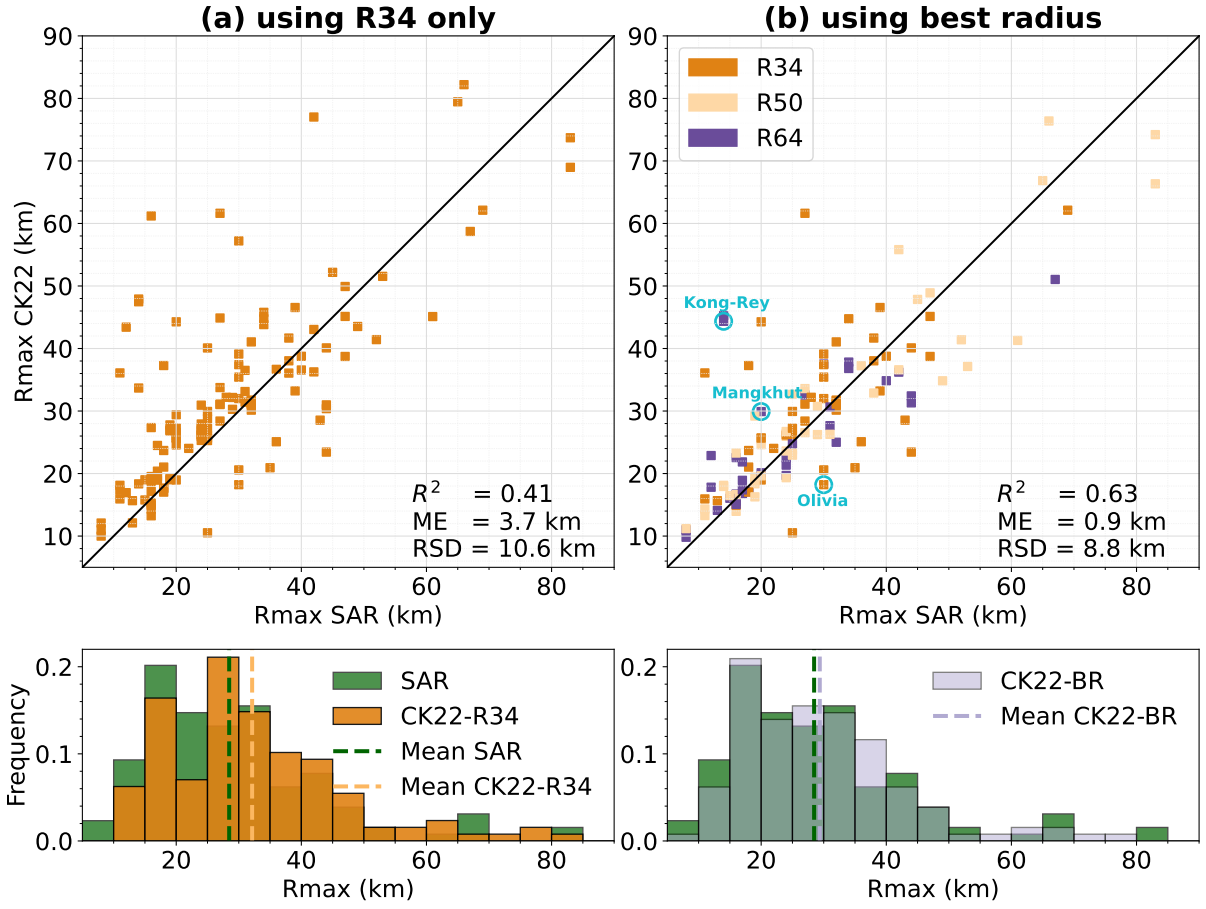


FIG. 5. Comparison between $R_{max}$ estimates using the CK22 model and SAR $R_{max}$ (top) and corresponding distributions (bottom) for $R_{max}^{CK22-R_{34}}$ (a) and $R_{max}^{CK22-BR}$ (b). For analysis purposes, color reveals which radius was used to define $R_{max}^{CK22-BR}$ for each case.

Because $R_{50}$ and $R_{64}$ are closer to $R_{max}$ than $R_{34}$, using one or the other wind radii thresholds should improve the quality of the ratio estimate compared to $R_{34}$. Ideally, an estimate of $R_{max}$ should be performed with $R_{64}$ if available. If $R_{64}$ is not defined (*i.e* if $V_{max}$ is less than 33 $ms^{-1}$),

$R_{50}$ should be used. $R_{34}$ should only be used if both $R_{64}$ and $R_{50}$ were not defined. Following this procedure, we further estimated $R_{max}$ using the "best" available wind radius.

Figure 5b shows a comparison between these estimates (hereafter $R_{max}^{CK22-BR}$) and SAR $R_{max}$. The $R^2$-score increased to 0.63 and the ME decreased to 0.9 $km$ compared to the $R_{max}^{CK22-R_{34}}$ methodology, while RSD decreased from 10.6 $km$ to 8.8 $km$. Therefore, using wind radii closer to $R_{max}$ does improve the estimate quality. In addition, such a low RSD demonstrates the efficiency of the fitted CK22 relationships (eqs. 3-5) to provide reliable $R_{max}$ estimates.

In their paper, the $R_{max}$ predicted by CK22 had a systematic bias that could be bias-adjusted in post-processing to improve the model. Here we find that our model does not require a bias adjustment, which may be an indication of the benefit of using direct observational data for $R_{max}$ (SAR).

While the method is successful on average, it is remarkable that errors can be large (more than $\sim$10 $km$), even for cases where $R_{64}$ predictors are used (see for instance Kong-Rey and Mangkhut in Fig. 5b). Before discussing how to explain these large uncertainties, a single TC life cycle was chosen to illustrate the potential of the present methodology.

### *c. Application to TC Kilo life cycle*

Producing $R_{max}^{CK22-BR}$ estimates every time a radiometer or a scatterometer TC overpass is available can be an efficient tool for characterizing the time evolution of $R_{max}$ for any given TC. Figure 6 shows TC Kilo $R_{max}$ and $V_{max}^{REG}$ time series between 27 August and 10 September 2015, a period over which $V_{max}^{REG}$ was larger than 20 $ms^{-1}$. TC Kilo evolved in the Pacific ocean, reaching category 4 on the Saffir-Simpson scale. It intensified from 20 to 49 $ms^{-1}$ between 27 August and 30 August before entering a weakening phase. In the meantime, $R_{max}$ first varied between 55 and 15 $km$ according to IBTrACS, then stagnated at 37 $km$ between the 30 August and the 2 September, before varying again after these date. Stagnation phases of $R_{max}$ from IBTrACS are likely not physical according to the $V_{max}^{REG}$ variations during that time interval (see section 5). $R_{max}^{CK22-BR}$ estimates show much more pronounced variations during those phases, with an increasing trend between 30 August and 8 September. This particular phase corresponds to an overall decrease of $V_{max}^{REG}$ and an overall increase of $R_{64}$ in our data (not shown), both of which would be expected to be associated with an increase in $R_{max}$.

For reference, 3 SAR $R_{max}$ estimates were available during TC Kilo's life cycle (green stars). The first SAR $R_{max}$ (10 $km$) on 27 August, doesn't match with our first estimate of $R_{max}$ (35 $km$). This illustrates the limitations of our proposed methodology and is discussed hereafter. The second and third SAR $R_{max}$ estimates are in better agreement with $R_{max}$ estimates, especially if we account for the overall $R_{max}$ trend given by our estimates.

Notably, there is more spread in the CK22 estimates on the last two days of the study period. Despite this increasing uncertainty, the increase of $R_{max}$ is well depicted, suggesting $R_{max}$ to significantly increase much before 8 September in contradiction with the IBTrACS trend.

In summary, every time a radiometer or scatterometer wind profile is available, a subsequent $R_{max}^{CK22-BR}$ estimate can be obtained, using the proposed objective method. In such a way, one can estimate $R_{max}$ trends that are more realistic than IBTrACS, less impacted from spatial or temporal heterogeneities. Such a framework could also be used operationally.

## 5. Discussion

The previous section demonstrated the potential of the CK22 model fitted with SAR, when used in combination with inter-calibrated medium-resolution radiometer and scatterometer data. Still, $R_{max}^{CK22-BR}$ estimates can display rather large uncertainties, despite the expected improved use of $R_{64}$ as predictor. To better understand the sources of such uncertainties, three other case studies (cyan circles on Fig. 5a) were considered before examining theoretical aspects and drawing a picture of the average situation.

### *a. Case studies from the SAR-radiometer dataset*

The first case (Fig. 7, left column) is TC Olivia in 2018, an Eastern Pacific ocean hurricane that reached category 4 on the Saffir-Simpson scale. It reached a first intensity peak (~56 $ms^{-1}$) on 5 September, then weakened before restrengthening (~59 $ms^{-1}$) during the night between 6 and 7 September. On 8 September, both RS2 at 1510 UTC and Windsat at 1533 UTC overflew Olivia (Figs. 7a and 7d). Its eyewall, depicted by the high-resolution SAR observation, was clearly defined though asymmetric. With its rather low spatial resolution, the radiometer failed to map the inner core areas with high wind speed gradients, and eyewall asymmetries. From the SAR observation, Olivia's $R_{max}$ was 30 $km$ at that time, with a $V_{max}$ of 32 $ms^{-1}$ (Fig. 7g). Notably,

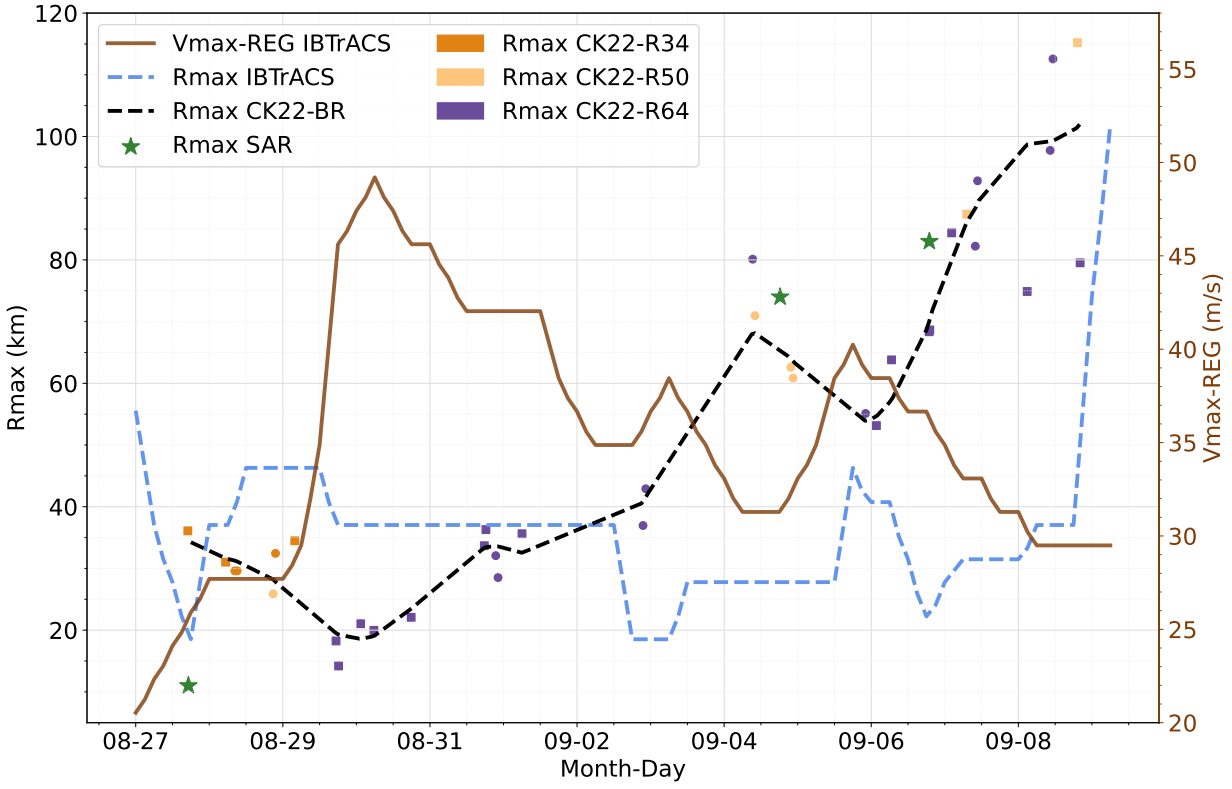


FIG. 6. Kilo (2015) time series of IBTrACS $R_{max}$ (left axis, dashed blue), radiometer- and scatterometer-based $R_{max}^{CK22-BR}$ (left axis, dashed black), and IBTrACS-based $V_{max}^{REG}$ (right axis, solid brown). Also displayed are radiometers (squares), scatterometers (circles) $R_{max}^{CK22-BR}$ estimates (color reveals which radius was used to define $R_{max}^{CK22-BR}$ for each observation), and SAR $R_{max}$ estimates (green stars). The dashed black line was obtained by applying a support vector regression to the radiometer- and scatterometer-based $R_{max}^{CK22-BR}$ estimates.

Windsat failed to estimate $V_{max}$ correctly, with a negative bias of almost 10 $ms^{-1}$, which is largely attributable to sensor spatial averaging effects. In fact, the entire azimuthally-averaged wind profile is negatively biased, leading to an underestimation of $R_{34}$, further reflected in $R_{max}^{CK22-BR}$. This case illustrates how wind radii uncertainties translate into $R_{max}^{CK22-BR}$ uncertainties.

The second case (Fig. 7, middle column), Mangkhut, was a super typhoon (category 5 on Saffir-Simpson scale), causing considerable damages in the Western Pacific ocean in 2018. It reached its peak intensity (~80 $ms^{-1}$) on 12 September. On 11 September, both S1B at 2048 UTC and Windsat at 2126 UTC overflew Mangkhut (Figs. 7b and 7e). According to the SAR observation, Mangkhut had a clearly-defined symmetric eyewall at that time. Note that the eyebrow shape near the eyewall (Fig. 7b) is probably due to rain contamination (for discussion about such a feature see Mouche

et al. (2019)). The extent of high winds was seemingly well captured by the radiometer sensor, but the eye was not resolved. Nevertheless, a very good agreement between S1B and Windsat wind outer-profiles is obtained for this case (Fig. 7h), with only ~3 $km$ error between $R_{64}$ estimates from the two sensors. Still, the estimate given by $R_{max}^{CK22-BR}$ (~30 $km$) largely overestimates the actual SAR $R_{max}$ (~20 $km$). With its large $R_{64}$ and small $R_{max}$ at that time, Mangkhut illustrates the high variability that occurs in nature. Such a case is likely to depart from any statistical relationship (like CK22) that links a wind radius to $R_{max}$.

The last case study (Fig. 7, right column), Kong-Rey, in 2018, was a super typhoon reaching category 5 on the Saffir-Simpson scale, also evolving over the Western North Pacific ocean. Following a ~72 $ms^{-1}$ peak intensity on 2 October Kong-Rey experienced an eyewall replacement cycle (ERC) and entered its weakening phase. Kong-Rey was captured on 2 October by both S1A at 2111 UTC and SMAP at 2133 UTC (Figs. 7c and 7f). The SAR observation depicts a well-defined symmetric eyewall, with a secondary ring of maximum winds further out from the TC center. In fact, Kong-Rey exhibited two eyewalls in 89 $GHz$ imagery at this time (not shown). These two high wind regions were not well captured by the radiometer. The radiometer wind profile saturates in the 80 $km$ inner-part of the TC, while the SAR wind profile exhibits two wind speed local maxima (Fig. 7i). Despite the inability of the radiometer sensor to capture the duel wind maxima observed at this time, the outer-part of the azimuthally-averaged wind profiles match well, both yielding a $R_{64}$ estimate of ~128 $km$. Though, $R_{max}^{CK22-BR}$ is 42 $km$, far from the 14 $km$ of SAR $R_{max}$. However, it is noteworthy that $R_{max}^{CK22-BR}$ lies between the two SAR wind maxima. The complex shape of Kong-Rey during its ERC is the main cause to explain such a huge discrepancy. Indeed, the $R_{64}$ estimate is pushed to an outer radius due to the existence of secondary wind maxima.

### *b. Structural aspects*

From these examples, we see that neither the use of high quality data (SAR) to train the algorithm nor the use of a radius that is very close to $R_{max}$ (*i.e* $R_{64}$) precludes large uncertainties of $R_{max}$ estimates using the CK22 framework. Underlying CK22, the use of an outer wind radius (*e.g* $R_{34}$[1]) to estimate $R_{max}$ is justified by the angular momentum conservation principle: an air parcel, advected from the outer radii to the innermost radii, must lose angular momentum due to surface friction. The ratio $\frac{M_{max}}{M_{34}}$ thus represents the ability for an air parcel to keep its angular momentum

[1]In this section we chose $R_{34}$ as outer wind radius for clarity, but the reasoning well applies to any other wind radius (*e.g* $R_{50}$ and $R_{64}$).

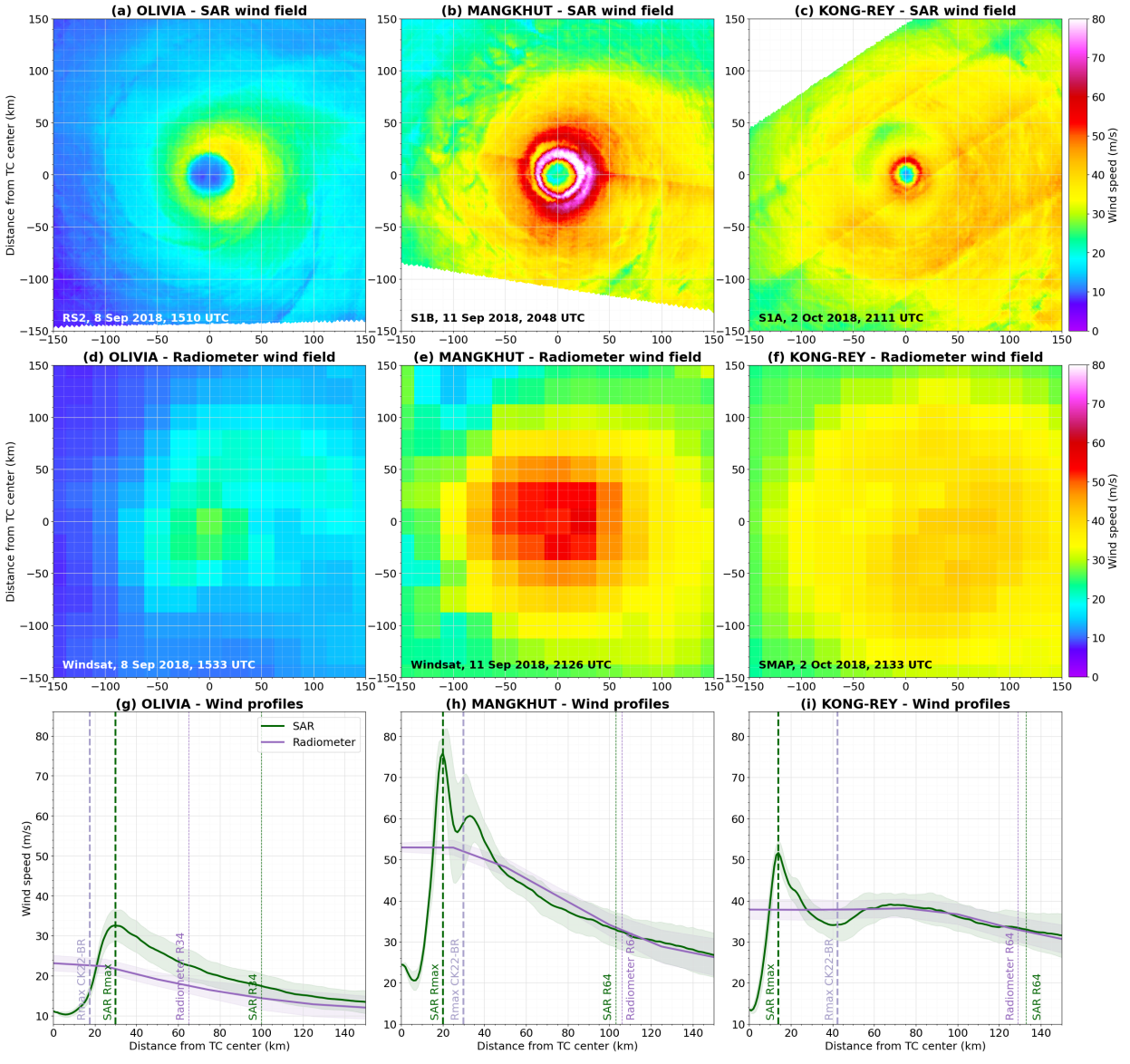


484 FIG. 7. Comparison of SAR and radiometer wind fields (top and middle rows, TCs are translating toward the top of each panel)
485 and corresponding wind profiles (bottom row) for Olivia (left column), Mangkhut (middle column) and Kong-Rey (right column).

493 while being advected from $R_{34}$ to $R_{max}$. In the log-linear framework, this ratio solely depends on
494 $V_{max}$, $R_{34}$, and $f$.

495 The use of these three parameters to estimate $\frac{M_{max}}{M_{34}}$ was discussed in Chavas et al. (2015) and
496 Chavas and Lin (2016). In these studies, the ability of a radial parametric wind profile to represent
497 the variability of observational data was tested. In brief, the radial parametric profile geometrically
498 merges an inner-part profile with an outer-part profile, previously anticipated from theoretical

studies (Emanuel and Rotunno 2011; Emanuel 2004). Chavas and Lin (2016) concluded that the ratio $\frac{M_{max}}{M_0}$ between the angular momentum at $R_{max}$ and at an outer-radius $R_0$ solely depends on four parameters: $V_{max}$, $fR_0$, $\frac{C_k}{C_d}$, and $\frac{W_{cool}}{C_d}$, where $C_k$ and $C_d$ are the heat and momentum exchange coefficients, while $W_{cool}$ models the radiative-subsidence rate in the free troposphere of the outer-part model. Considering $R_0 = R_{34}$, a log-linear dependence of $\frac{M_{max}}{M_{34}}$ on ($V_{max}$, $R_{34}$, $f$) thus neglects the variations of both $\frac{C_k}{C_d}$ and $\frac{W_{cool}}{C_d}$.

Besides, the axisymmetric and steady-state theory of Emanuel and Rotunno (2011) invokes a direct relationship between $\frac{M_{max}}{M_{34}}$ and $\frac{C_k}{C_d}$, that can be stated as

$$\frac{M_{max}}{M_{34}} = \pi(\frac{C_k}{C_d}) \tag{6}$$

with $\pi(x) := (\frac{1}{2}x)^{\frac{1}{2-x}}$ a monotonically increasing function (see their eq. 38). This relationship assumes the TC is in steady-state and the Richardson number in the outflow is slightly below one. The latter implies the outflow is self-stratified by small-scale turbulence. Using numerical simulations that resolved convection, Emanuel and Rotunno (2011) showed that such an assumption was satisfied in an outflow region near $R_{max}$. This assumption might then not hold true further out. Chavas et al. (2015) suggested that the optimal merging radius between the inner- and outer-part of the model was $\sim 2-3R_{max}$ when fitting the complete parametric profile to observational data. While not strictly corresponding to the region where the theoretical developments of Emanuel and Rotunno (2011) could remain valid, it identifies the region where the inner-part of the model is most likely to apply to the observations.

When writing eq. 6, one assumes that the model of Emanuel and Rotunno (2011) is still valid at $R_{34}$, which largely exceeds $3R_{max}$ in nature. This might be a strong approximation, but it offers an instructive relationship between the rate of conservation of angular momentum (left-hand side) to a function of $\frac{C_k}{C_d}$, characterizing the balance between energy generation and friction loss (right-hand side). Most importantly, $\frac{C_k}{C_d}$ controls the shape of the parametric radial wind profile, with higher values corresponding to more peaked profiles. In practice, unlike $\frac{C_k}{C_d}$ values, this shape of the near-peak radial wind profile is more easily quantifiable using SAR data.

To highlight these considerations, we present TC cases that have the same CK22 predictors ($V_{max}$, $R_{64}$, $f$) but different wind profile shapes near their peak intensities. Figure 8 is representative of such a situation. SAR acquisitions over TC Rammasun (West Pacific, red curve) and TC Marie

(East Pacific, blue curve), occurred on 17 July 2014 at 1027 UTC and on 3 October 2020 at 1419 UTC, respectively. Both storms display similar outer-core profiles, with almost the same $R_{64}$ (~52 and ~49 $km$), $V_{max}$ (~42 and ~43 $m.s^{-1}$) and $f$ (~4.3 and ~4.6 $s^{-1}$). Applying CK22 to these cases (vertical dashed lines) thus leads to almost the same $R_{max}^{CK22-BR}$ value (~25 and ~22 $km$). However, SAR derived wind profiles provide different estimates, $R_{max}$ (~34 and ~24 $km$, respectively).

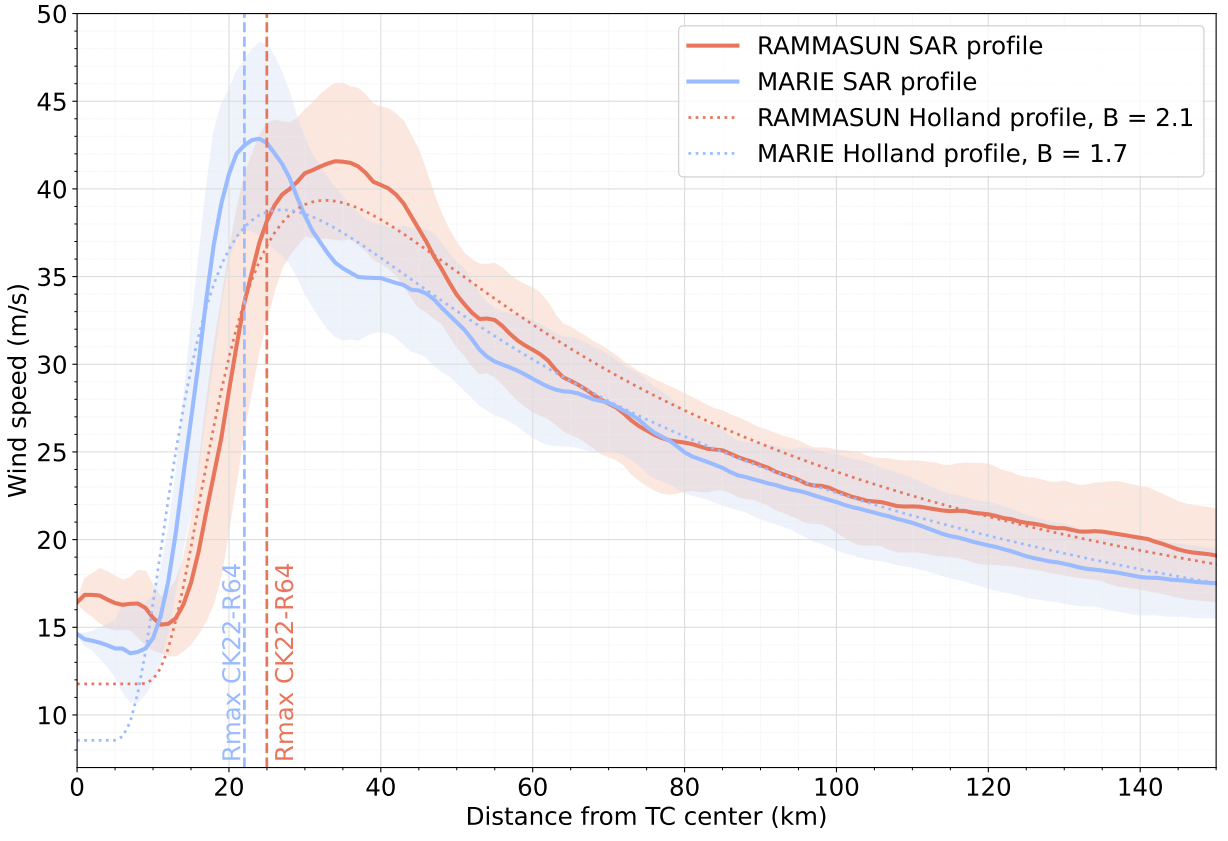


FIG. 8. SAR wind profiles for Rammasun (solid red) and Marie (solid blue) and associated Holland best-fit profiles (dotted curves) fitted on $0 \leq r \leq 500km$.

Comprehensively, the CK22 model cannot fully adjust to peculiar local wind profiles. To quantify the wind profile shapes, a Holland parametric profile (Holland 1980) was adjusted to each SAR azimuthally-averaged wind profile:

$$V_{Holland}(r) = V_{min} + \sqrt{(V_{max} - V_{min})^2 (\frac{R_{max}}{r})^B e^{1-(\frac{R_{max}}{r})^B} + (\frac{rf}{2})^2} - \frac{rf}{2} \quad (7)$$

This parametric formulation is useful to quantify variations in the shape of observed wind profiles. In particular, the empirical B parameter controls the rate of radial decay of the tangential winds, with higher (smaller) values corresponding to narrower (broader) vortices. In addition, this parameter was found to be sensitive to TC intensity and size while independent of $R_{max}$ (Knaff et al. 2011).

Note, Holland's profiles were designed for gradient-level wind and are not necessarily suited for surface wind profiles with nonzero wind speeds at the TC center, well captured using SAR observations. A complementary degree of freedom ($V_{min}$) was thus included in eq. 7 to cope with the existence of nonzero minimum wind speeds.

Using the full extent of the wind profile, a solution for $V_{min}$, $V_{max}$, $R_{max}$ and $B$ can be estimated via least squares. Applied to TC Rammasun and Maria, the fitting procedure results in two different $B$ values, ~2.1 and ~1.7, respectively (Fig. 8). Such a difference quantifies the remaining variability of the near-core wind profile for comparable outer-core wind profiles.

### *c. Analysis framework*

The shape of the near-core wind profile is generally associated with the radial gradient of absolute angular momentum and thus the loss of angular momentum when an air parcel is advected from $R_{34}$ to $R_{max}$. To guide the analysis, we recall the equation of angular momentum conservation for an axi-symmetric vortex:

$$\frac{\partial M}{\partial t} + u\frac{\partial M}{\partial r} + w\frac{\partial M}{\partial z} = \frac{r}{\rho}\frac{\partial \tau_{\theta z}}{\partial z} \tag{8}$$

with $u$ and $w$, the radial and vertical velocities, $\tau_{\theta z}$ a tangential stress component, and $\rho$ the density. The continuity equation links $u$ and $w$ as

$$\frac{1}{r}\frac{\partial (ru)}{\partial r} + \frac{\partial w}{\partial z} = 0 \tag{9}$$

Under steady state condition, eq. 8 can be integrated from the surface to a boundary layer height, $h$, where the stress vanishes:

$$\int_0^h u\frac{\partial M}{\partial r}\,dz + \int_0^h w\frac{\partial M}{\partial z}\,dz = -\frac{r\tau_{\theta s}}{\rho} = -C_d r V^2 \tag{10}$$

with $\tau_{\theta s} \approx C_d \rho V^2$ the surface stress, $C_d$ a drag coefficient and $V$ the tangential surface wind component. Assuming $w(z=0) = 0$ and the use of the continuity equation (eq. 9), the second term of the left hand-side in eq. 10 is integrated by parts, following developments presented by Kalashnik (1994), to obtain

$$\int_0^h u \frac{\partial M}{\partial r}\, dz + [wM]|_{z=h} + \int_0^h \frac{M}{r} \frac{\partial (ru)}{\partial r}\, dz = -C_d r V^2 \tag{11}$$

Grouping the two integrals yields

$$\frac{1}{r} \frac{d}{dr} \left( r \int_0^h uM\, dz \right) + [wM]|_{z=h} = -C_d r V^2 \tag{12}$$

Defining $\overline{u} := \frac{1}{h} \int_0^h u\, dz$ we can approximate the integral $\int_0^h uM\, dz \approx h\overline{u}M|_{z=h}$ and rewrite the continuity equation $w|_{z=h} = -\frac{h}{r} \frac{d}{dr}(r\overline{u})$. Rearrangement finally yields:

$$rV^2 \approx -\frac{h\overline{u}}{C_d} \frac{dM}{dr} \tag{13}$$

where $\frac{dM}{dr}$ is the radial gradient of absolute angular momentum at the top of the boundary layer. Assuming the latter closely related to its value at the surface, eq.13 then explicitly links the shape of the wind profile $\frac{dM}{dr}$ to $rV^2$.

Using SAR measurements, both quantities can be accurately estimated, and the validity of eq. 13 assessed. Figure 9a represents $R_{max}V_{max}^2$ (y-axis) as a function of $R_{34}V_{34}^2$ (x-axis) and colored by the fitted $B$ values[2]. On average, *i.e* $B \simeq 1.8$, a relationship emerges when comparing $R_{max}V_{max}^2$ and $R_{34}V_{34}^2$. Departures from a one-to-one relationship, related to conservation of the $rV^2$ parameter, are seemingly well explained by $B$ values. Large $B$, corresponding to very peaked wind profiles near $V_{max}$, leads to larger $R_{max}V_{max}^2$ for a given $R_{34}V_{34}^2$. For broader wind profiles, corresponding to smaller $B$, smaller $R_{max}V_{max}^2$ are generally found.

Moreover, the space spanned in the ($R_{34}V_{34}^2$, $R_{max}V_{max}^2$)-plane is still apparently large, even at constant $B$. From eq. 13, this increased variability is possibly associated with the factor $\frac{h\overline{u}}{C_d}$. Overall, these results suggest that the variability encountered in nature does not solely depends on the three predictors ($V_{max}$, $R_{34}$, $f$).

[2] $B$, as a scalar value, was used instead of a criterion based on $\frac{dM}{dr}$ to describe the shape of the wind profile

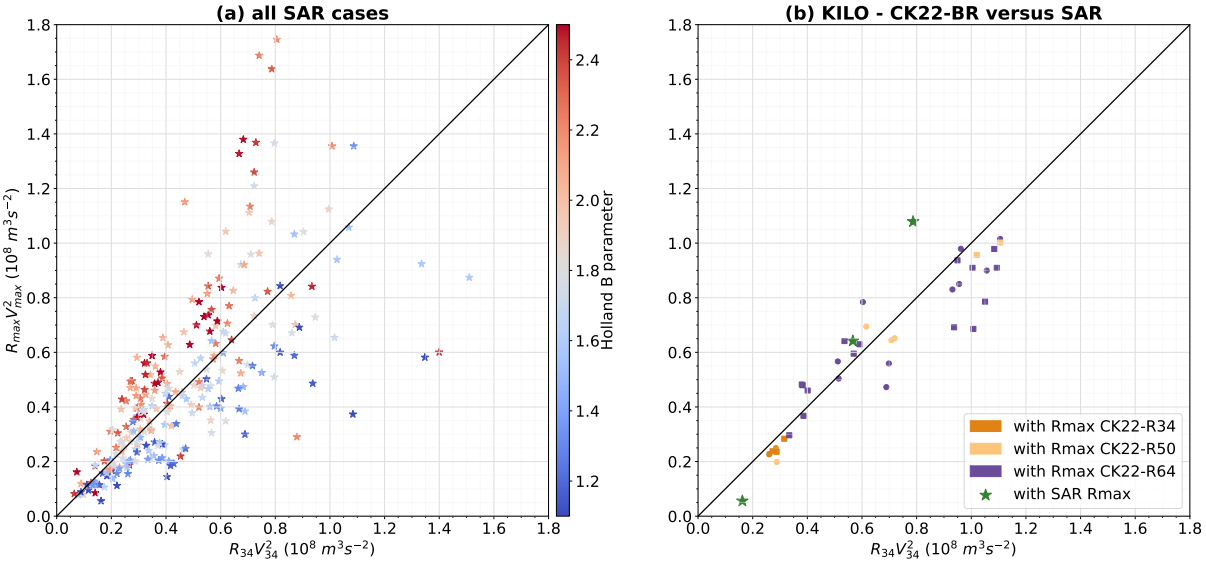


FIG. 9. Evaluation of the PV conservation assumption in the SAR dataset (a) and for Kilo's life cycle (b) using $R_{34}$ estimated on radiometer and scatterometer data along with corresponding $R_{max}^{CK22-BR}$ estimates and $V_{max}^{REG}$. The three SAR cases (green stars) are also displayed for reference.

To further illustrate this diagnosis, Fig. 9b displays the same ($R_{34}V_{34}^2$, $R_{max}V_{max}^2$)-plane, but using the radiometer and scatterometer database, and corresponding $V_{max}^{REG}$, $R_{34}$ and $R_{max}^{CK22-BR}$ estimates. As expected, the variability captured by using $R_{34}$ or $R_{50}$ to estimate $R_{max}$ via CK22 is poor. While using $R_{64}$ increases this variability, the overall spread is reduced compared to Fig. 9a, suggesting that the variability of the wind profile shapes associated with the $R_{max}^{CK22-BR}$ estimates is low.

Note, the average situation $rV^2 \approx$ constant which is depicted in our study thanks to the SAR database has already been discussed by Riehl (1963) when he argued that PV is conserved within the inflow layer. PV conservation implies the vertical component of the curl of the frictional force to be zero, or

$$\frac{r}{\rho}\frac{\partial \tau_{\theta z}}{\partial z} = \text{constant} \tag{14}$$

Integrating this equation over the boundary layer height yields (assuming constant density):

$$\frac{r\tau_{\theta s}}{\rho} = C_d r V^2 = \text{constant} \tag{15}$$

Thus, for a constant or slowly varying drag coefficient $C_d$, PV conservation leads to $rV^2 \approx$ constant (Riehl 1963). Mentioned above, such a relationship is, on average, consistent with the SAR estimates. However, for this relationship, the only source of variability comes from $C_d$. From arguments raised above (eq. 13), $h$ and $\overline{u}$ should also be further considered.

Lastly, one limitation of our observational analysis is that SAR $V_{max}$ is an estimate of the maximum total wind speed rather than the maximum tangential wind speed. Knowing how the total wind speed is distributed between its tangential and radial component near the eyewall region would allow to better estimate the impact of $\overline{u}$ on PV conservation and its variability.

### *d. Comparison of $R_{max}^{CK22-BR}$ with existing $R_{max}$ estimates*

With these results in mind, we assessed how much $R_{max}^{CK22-BR}$ estimates improved existing $R_{max}$ estimates. Figure 10 displays density contours of ($V_{max}$, $R_{max}$) joint distributions using IBTrACS $R_{max}$ (dashed blue) or $R_{max}^{CK22-BR}$ estimates (solid black). For comparison, the same density contours are shaded for the SAR dataset (green).

We remind readers that SAR wide-swaths acquisitions cannot be continuously performed over the ocean. As a consequence, not only does the SAR dataset contain much fewer cases, it is also biased towards higher intensities. Indeed, acquisition orders are most often requested to observe higher intensity systems. Thus, for the lowest $V_{max}$ (less than $\sim 30\ ms^{-1}$), possible inconsistencies in $R_{max}$ densities arise when comparing SAR to radiometer and scatterometer or IBTrACS. The density contours suggest that both IBTrACS $R_{max}$ and $R_{max}^{CK22-BR}$ estimates are larger than SAR $R_{max}$, while, in fact, this is just a consequence of the lack of SAR data at these intensities.

Nevertheless, and more importantly for high surface winds, discrepancies in $R_{max}$ densities are observed. Indeed, on average IBTrACS density contours are centered on a higher $R_{max}$ ($\sim$30 $km$) than SAR (progressively decreasing to $\sim$20 $km$). Confirming the efficacy of the revised model, radiometer- and scatterometer-based density contours display an average $R_{max}^{CK22-BR}$ ($\sim$20 $km$) that is consistent with SAR $R_{max}$. Depicted by the $R_{max}$ density curves (right panel), for low $R_{max}$, IBTrACS density is lower than both SAR and $R_{max}^{CK22-BR}$ values.

For further comparison, we computed $R_{max}$ estimates from $R_{34}$ on the radiometer and scatterometer data using eq. 7 of Chavas and Knaff (2022). The corresponding density curve (dotted red) shows only a minor improvement compared to IBTrACS at low $R_{max}$.

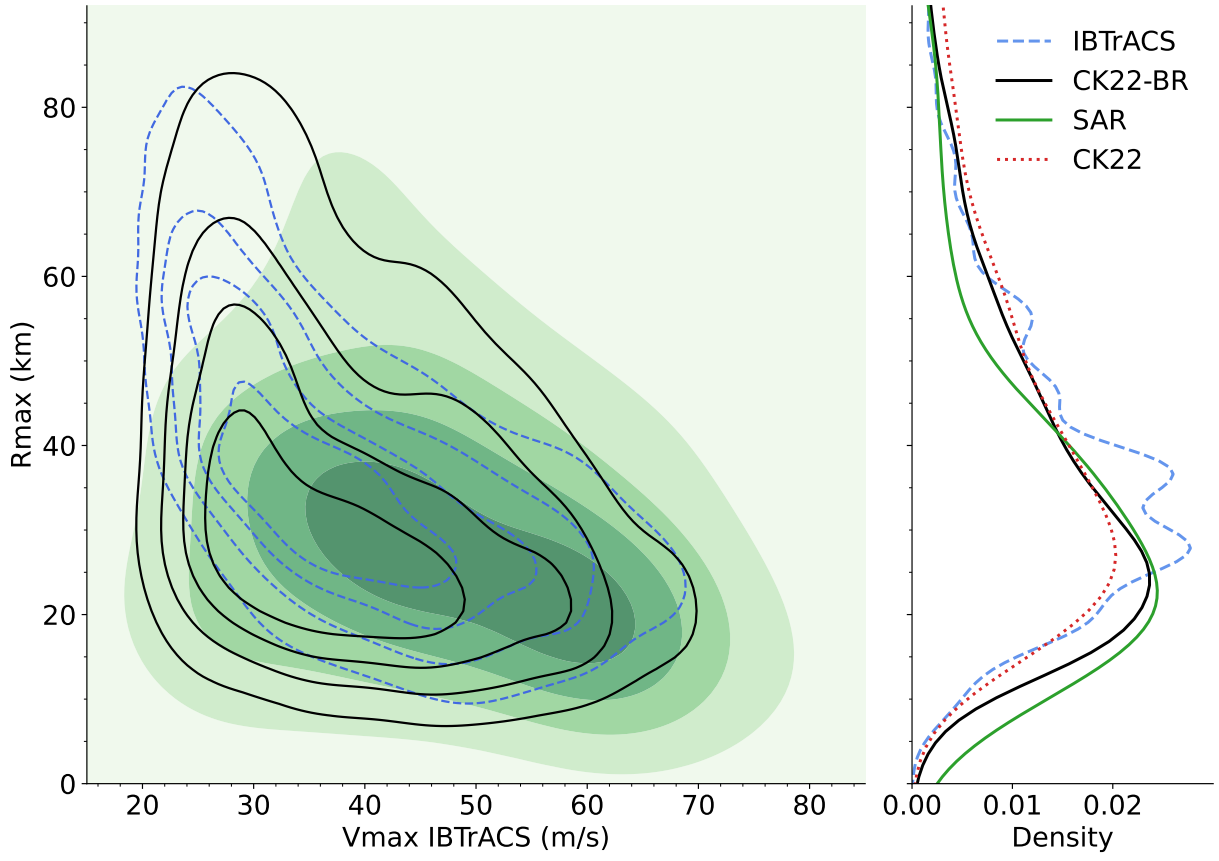


FIG. 10. Density contours of ($V_{max}$, $R_{max}$) joint distribution for the SAR dataset (shaded green, $V_{max}$ based on IBTrACS), for the dataset based upon radiometers and scatterometers with $R_{max}^{CK22-BR}$ (solid black) and based on corresponding IBTrACS $R_{max}$ values (dashed blue). The corresponding $R_{max}$ density curves are displayed on the right panel, along with $R_{max}$ estimates obtained by applying eq. 7 of Chavas and Knaff (2022) to the radiometer- and scatterometer-based dataset (dotted red).

Finally, the density contours of the radiometer and scatterometer dataset with $R_{max}^{CK22-BR}$ span a larger space than IBTrACS in the ($V_{max}$, $R_{max}$)-plane. This shows that the former captures more variability than best-track data. This is likely due to the use of $R_{64}$ in the regression, a result already suggested by Fig. 9b. Even though the datasets don't have the same $V_{max}$ distributions, Fig. 10 also suggests that the radiometer and scatterometer density contours span less space than SAR observations in the ($V_{max}$, $R_{max}$)-plane. While this is consistent with the above analysis, more SAR cases are needed to properly interpret Fig. 10.

## 6. Conclusions and perspectives

Understanding TC intensity changes certainly remains an observationally challenging problem. As expressed during the Tenth International Workshop on Tropical Cyclones (IWTC-10, recommendation 4), both the operational and research communities recognize the need for more homogeneous and standardized datasets for TC wind structure parameters, such as $R_{max}$ and the wind radii. The fact that $R_{34}$ was not systematically reanalyzed in all basins, and that $R_{max}$ is still not reanalyzed today (best-track $R_{max}$ value typically stems from its operational estimate) hampers the consolidation of such a dataset. Systematic and standardized wind radii are needed when using, and further improving, a semi-empirical model such as CK22. Although satellite sensors have their limitations, especially regarding the inter-calibration of different missions and sensors, resulting multi-modal observations shall serve for such a systematic and global approach, at least for wind radii estimation.

More specifically and thanks to high-resolution (SAR) data, it is now possible to more systematically estimate $R_{max}$. Fitted with SAR estimates and used in conjunction with the closest wind radius to $R_{max}$, our study proposed a revised CK22 model. It is shown to be an efficient tool to provide improved reliable estimates, with an average uncertainty of $\sim 9\ km$. Because outer-core wind radii can be estimated from radiometer or C-band scatterometer data, the developed framework thus allows to produce a more extensive dataset of reanalyzed $R_{max}$ estimates. The resulting time series are generally more realistic than those obtained from best-track $R_{max}$ estimates. The method can also be used to provide operational guidance on the location of the maximum intensity every time a radiometer or C-band scatterometer overflies the TC, as long as its intensity and location are also estimated, noting that such estimates are routinely available from operational centers. Furthermore, the proposed method could also be used to guide the best-tracking process when no reliable $R_{max}$ observation is available.

The efficacy of the semi-empirical CK22 model stems from fundamental conservation principles. Indeed, the high-resolution SAR database highlights that TCs, on average, conserve their PV, with a resulting approximation $rV^2 \approx$ constant. Accordingly, the use of CK22 to retrieve $R_{max}$, based on an outer-radius wind observation coupled with an intensity estimate is, on average, justified. Single cases can still depart considerably from the PV conservation assumption, especially those

at very high intensity ($V_{max}$) or with large inner- ($R_{max}$) or outer-size ($R_{34}$). And, to first order, those deviations are well explained by variations of the observed wind profile shapes.

While the use of $R_{64}$ can account for some of the deviations due to the radial gradient of absolute angular momentum, the CK22 model seems to fail to capture the remaining variability observed in the SAR database. Large variability is apparently still occurring near the TC core. To further advance our understanding, there continues to be a need for spaceborne SAR and airborne SFMR sensors as these are the only tools that resolve surface winds in this area. Both sensors however suffer from a lack of spatio-temporal sampling, and airborne measurements suffer from a lack of azimuthal coverage. The future is bright with the recently launched RADARSAT Constellation Mission (RCM) operated by CSA, which should improve the satellite SAR spatio-temporal sampling. RCM has already proved useful by providing significantly more $R_{max}$ estimates than anticipated for the 2022-2023 season. And, increasing the number of available SAR cases will certainly allow to better understand how absolute angular momentum gradients are constrained in the near-core region.

Furthermore, the integrated equations show that both the boundary layer depth ($h$), the average radial inflow ($\overline{u}$), and the drag ($C_d$) also impact the relationship between PV conservation and the near-core wind profile shape. While the $C_d$ behaviour under very high winds is still actively debated (Powell et al. 2003; Bell et al. 2012), measurements of both $h$ and $\overline{u}$ may be facilitated by the Doppler-based motions derived from the Imaging Wind and Rain Airborne Profiler (IWRAP) instrument (Sapp et al. 2022). For the radial inflow, improved estimates at the surface, in the near-core region, shall be made possible with the future Harmony mission (ESA 2022), the ESA Earth Explorer 10. This mission will augment Sentinel 1D observations with two satellite companions, providing azimuth diversity from these bi-static observations. In addition, the Second Generation Meteorological Operational satellite programme (Metop-SG) will operate in both co- and cross-polarization. Unlike the current spaceborne instruments, ASCAT, which have only co-polarization measurements, the higher sensitivity of cross-polarized signals to ocean breaking waves may thus improve the ocean surface wind vectors measured by scatterometers, approaching the TC core regions. Also, the coming Copernicus Imaging Microwave Radiometer (CIMR) promises to offer large swath with improved resolution, low uncertainty observation capabilities, combining L-, C- and X-band frequencies . The presence of 1.4 GHz L-band channel on board CIMR will open

up the possibility to further interpret the high-resolution C- and X-band measurements, to provide improved surface wind vector estimates under extreme conditions (Kilic et al. 2018).

Finally, in the absence of high-resolution observations, the shape of the near-core wind profile may also be indirectly estimated. Given the relation $rV^2 \approx$ constant under a steady-state assumption, a departure from this relation can help understand the temporal variations of absolute angular momentum. Estimates of these temporal variations may then be used to evaluate how much the near-core wind profile shape departs from the average relationship. The wind profile shape is also linked to the drag coefficient (see for instance the steady-state view of Emanuel and Rotunno (2011)), which modulates asymmetries in the boundary layer response (Shapiro 1983; Kepert 2001). Asymmetries possibly captured by medium- or low-resolution observations (scatterometers or radiometers), may thus help to infer boundary layer frictional drag terms, and to quantify the resulting shape of the wind profile.

*Acknowledgments.* This work was financially supported by the ERC Synergy project 856408-STUOD, the ANR projects OceaniX and ISblue, and the ESA Marine Atmosphere eXtreme Satellite Synergy project (MAXSS). The radiometer and scatterometer dataset used in this report is part of the MAXSS project. The SAR database was obtained from IFREMER/CyclObs and produced with the SAR wind processor co-developed by IFREMER and CLS. J. Knaff thanks NOAA/Center for Satellite Applications and Research for providing the time work on this subject. The views, opinions, and findings contained in this report are those of the authors and should not be construed as an official National Oceanic and Atmospheric Administration or U.S. government position, policy, or decision.

*Data availability statement.* The data used in this study are freely available online for both the dataset of radiometer and scatterometer winds (`https://www.odatis-ocean.fr/donnees-et-services/acces-aux-donnees/catalogue-complet/#/metadata/6c56bcde-050f-42eb-92b8-8e882e1f4db9`) and the SAR database (`https://cyclobs.ifremer.fr/`).

## APPENDIX A

### Scatterometer wind speed estimates

As explained in section 2, the wind speed estimates from different radiometer and scatterometer sensors have been inter-calibrated prior to our study. During this process, the C-band ASCAT missions were calibrated using a 25 $km$ resolution, while the Ku-band scatterometer sensors were calibrated using a 50 $km$ resolution. Spatial resolution was already demonstrated to impact how well TCs intensities are resolved in numerical models (Davis 2018) and observations (Quilfen et al. 1998). Here, we expect discrepancies between the C- and Ku-band observational wind products.

To quantify this resolution effect, SAR wind fields were degraded to both 25 and 50 $km$ spatial resolution and then azimuthally-averaged. The $V_{max}$ values estimated from these degraded wind profiles were then compared to IBTrACS $V_{max}$, as represented by the green (25 $km$) and red (50 $km$) stars of Fig. A1. Here, SAR $V_{max}$ refers to the maximum found in an azimuthally-averaged wind profile. We thus expect slight discrepancies with IBTrACS $V_{max}$, whose definition does not strictly coincide with a wind profile maximum. The comparison between SAR azimuthal means

and IBTrACS is indicated by the grey stars and modelled by a linear fit (grey dashed line in Fig. A1) which defines $V_{max}^{REG}$:

$$V_{max}^{REG} = 0.6967 V_{max}^{IBTrACS} + 6.1992 \quad \text{(A1)}$$

The green and red scatters in Fig. A1 should be compared to this regression line (grey dashed) rather than the 1:1 line. The 25- and 50-$km$ simulated $V_{max}$ values show that as spatial resolution decreases $V_{max}$ also decreases, and the decreasing tendency is more pronounced as intensity increases. On average, a $V_{max}$ of ~38 $ms^{-1}$ observed at the full-resolution azimuthally-averaged wind profile (*i.e* the raw SAR wind profile) would yield ~32 $ms^{-1}$ when observed at a 25 $km$ spatial resolution and ~28 $ms^{-1}$ at a 50 $km$ spatial resolution. Second-order polynomial fits were constructed to model this spatial resolution effect.

Using these linear and polynomial fits as reference, we then compared C-band and Ku-band scatterometer $V_{max}$ values with IBTrACS in Fig. A2. It shows that C-band scatterometer $V_{max}$ values are consistent with the 25 $km$ spatial resolution polynomial model (green dashed curve). In contrast, Ku-band scatterometer $V_{max}$ are still underestimated when compared to IBTrACS values following the correction for their 50 $km$ resolution (red dashed curve). In particular, Ku-band scatterometer $V_{max}$ estimates rarely exceed 64 knots (33 $ms^{-1}$), precluding their use to estimate wind radii in our analysis.

## References


Bell, M. M., M. T. Montgomery, and K. A. Emanuel, 2012: Air–sea enthalpy and momentum exchange at major hurricane wind speeds observed during cblast. *Journal of the Atmospheric Sciences*, **69 (11)**, 3197–3222.

Brennan, M. J., C. C. Hennon, and R. D. Knabb, 2009: The operational use of quikscat ocean surface vector winds at the national hurricane center. *Weather and Forecasting*, **24 (3)**, 621–645.

Chavas, D. R., and J. A. Knaff, 2022: A simple model for predicting the tropical cyclone radius of maximum wind from outer size. *Weather and Forecasting*, **37 (5)**, 563–579.

Chavas, D. R., and N. Lin, 2016: A model for the complete radial structure of the tropical cyclone wind field. part ii: Wind field variability. *Journal of the Atmospheric Sciences*, **73 (8)**,

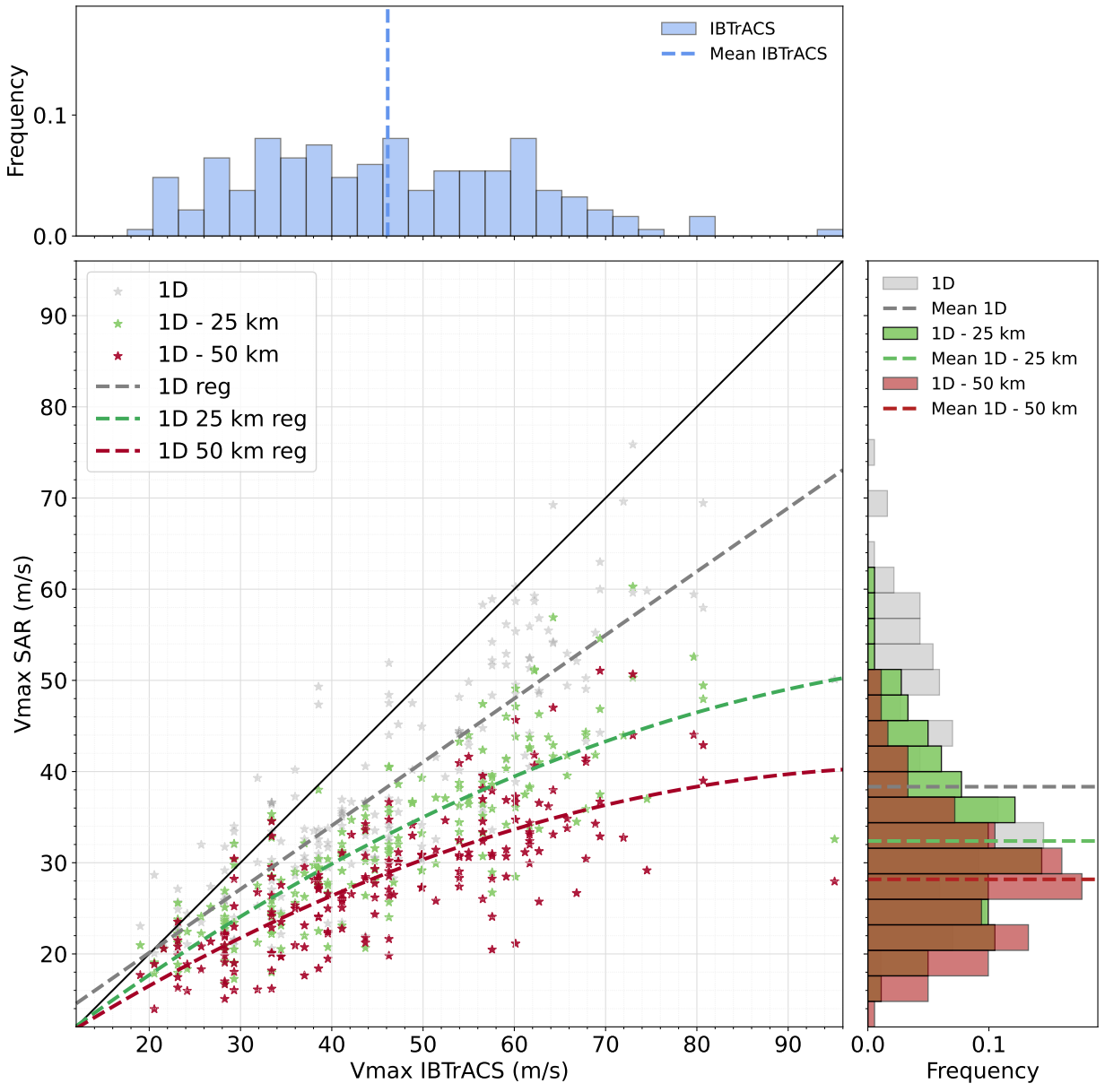


742 FIG. A1. Comparison between SAR (y-axis) and IBTrACS (x-axis) $V_{max}$ for the raw dataset (grey) and when degraded at
743 25 $km$ (green) or 50 $km$ (red) resolution. Dashed lines represent best linear fit for the raw dataset (grey) and best second order
744 polynomial fits for the 25 $km$ (green) and 50 $km$ (red) datasets. A solid black line represents identity. $V_{max}$ distributions and
745 averages are displayed for the different SAR samples (right) and for corresponding IBTrACS values (top).

766 3093–3113.

767 Chavas, D. R., N. Lin, and K. Emanuel, 2015: A model for the complete radial structure of
768 the tropical cyclone wind field. part i: Comparison with observed structure. *Journal of the*

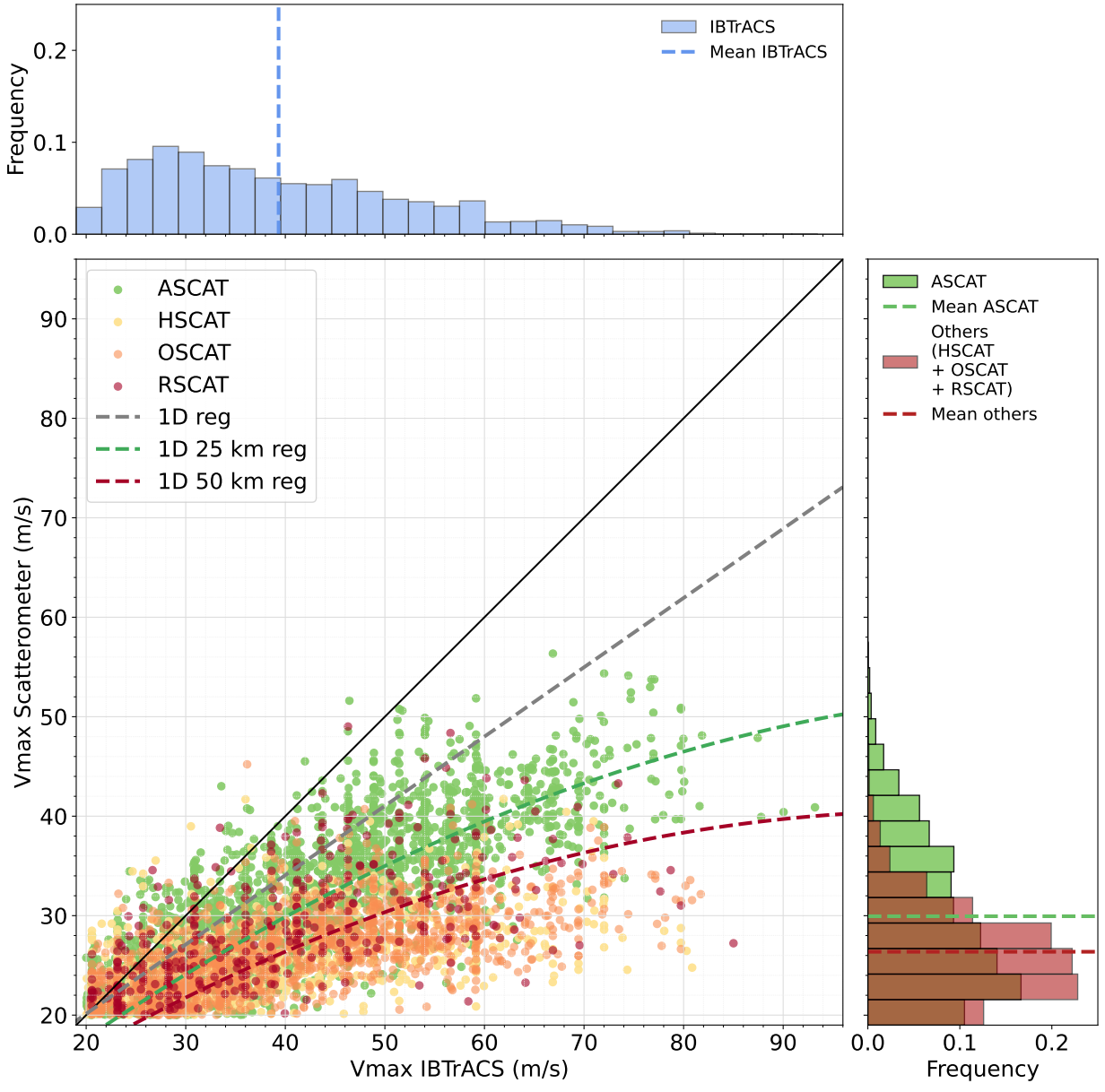


FIG. A2. Comparison between scatterometer (y-axis) and IBTrACS (x-axis) $V_{max}$ for ASCAT (green), HSCAT (yellow), OSCAT (orange), and RSCAT (red). Solid and dashed lines are identical to Fig. A1. $V_{max}$ distributions and averages are displayed for the different scatterometer datasets (right) and for corresponding IBTrACS values (top).

*Atmospheric Sciences*, **72 (9)**, 3647–3662.

Chou, K.-H., C.-C. Wu, and S.-Z. Lin, 2013: Assessment of the ascat wind error characteristics by global dropwindsonde observations. *Journal of Geophysical Research: Atmospheres*, **118 (16)**, 9011–9021.

Combot, C., A. Mouche, J. Knaff, Y. Zhao, Y. Zhao, L. Vinour, Y. Quilfen, and B. Chapron, 2020a: Extensive high-resolution synthetic aperture radar (sar) data analysis of tropical cyclones: Comparisons with sfmr flights and best track. *Monthly Weather Review*, **148 (11)**, 4545–4563.

Combot, C., Y. Quilfen, A. Mouche, J. Gourrion, C. de Boyer Montégut, B. Chapron, and J. Tournadre, 2020b: Space-based observations of surface signatures in the wakes of the 2018 eastern pacific tropical cyclones. *Journal of Operational Oceanography*, **13 (Suppl. 1)**.

Davis, C., 2018: Resolving tropical cyclone intensity in models. *Geophysical Research Letters*, **45 (4)**, 2082–2087.

Donnelly, W. J., J. R. Carswell, R. E. McIntosh, P. S. Chang, J. Wilkerson, F. Marks, and P. G. Black, 1999: Revised ocean backscatter models at c and ku band under high-wind conditions. *Journal of Geophysical Research: Oceans*, **104 (C5)**, 11 485–11 497.

Emanuel, K., 2004: Tropical cyclone energetics and structure. *Atmospheric turbulence and mesoscale meteorology*, **165**, 192.

Emanuel, K., and R. Rotunno, 2011: Self-stratification of tropical cyclone outflow. part i: Implications for storm structure. *Journal of the Atmospheric Sciences*, **68 (10)**, 2236–2249.

ESA, 2022: Report for mission selection: Earth explorer 10 candidate mission harmony. Tech. rep., ESA, Noordwijk, The Netherlands, 369 pp.

Ginis, I., 2002: Tropical cyclone-ocean interactions. *Advances in Fluid Mechanics Series*, **33**.

Holland, G. J., 1980: An analytic model of the wind and pressure profiles in hurricanes.

Irish, J. L., D. T. Resio, and J. J. Ratcliff, 2008: The influence of storm size on hurricane surge. *Journal of Physical Oceanography*, **38 (9)**, 2003–2013.

Kalashnik, M., 1994: On the maximum wind velocity in the tropical cyclone. *Izvestiâ Akademii nauk SSSR. Fizika atmosfery i okeana*, **30 (1)**, 26–30.

Kepert, J., 2001: The dynamics of boundary layer jets within the tropical cyclone core. part i: Linear theory. *Journal of the Atmospheric Sciences*, **58 (17)**, 2469–2484.

Kilic, L., and Coauthors, 2018: Expected performances of the copernicus imaging microwave radiometer (cimr) for an all-weather and high spatial resolution estimation of ocean and sea ice parameters. *Journal of Geophysical Research: Oceans*, **123 (10)**, 7564–7580.

Klotz, B. W., and E. W. Uhlhorn, 2014: Improved stepped frequency microwave radiometer tropical cyclone surface winds in heavy precipitation. *Journal of Atmospheric and Oceanic Technology*, **31 (11)**, 2392–2408.

Knaff, J. A., C. R. Sampson, P. J. Fitzpatrick, Y. Jin, and C. M. Hill, 2011: Simple diagnosis of tropical cyclone structure via pressure gradients. **26**, 1020 – 1031, https://doi.org/https://doi.org/10.1175/WAF-D-11-00013.1.

Knaff, J. A., and Coauthors, 2021: Estimating tropical cyclone surface winds: Current status, emerging technologies, historical evolution, and a look to the future. *Tropical Cyclone Research and Review*, **10 (3)**, 125–150.

Knapp, K. R., M. C. Kruk, D. H. Levinson, H. J. Diamond, and C. J. Neumann, 2010: The international best track archive for climate stewardship (ibtracs) unifying tropical cyclone data. *Bulletin of the American Meteorological Society*, **91 (3)**, 363–376.

Kossin, J. P., J. A. Knaff, H. I. Berger, D. C. Herndon, T. A. Cram, C. S. Velden, R. J. Murnane, and J. D. Hawkins, 2007: Estimating hurricane wind structure in the absence of aircraft reconnaissance. *Weather and Forecasting*, **22 (1)**, 89–101.

Kudryavtsev, V., A. Monzikova, C. Combot, B. Chapron, and N. Reul, 2019: A simplified model for the baroclinic and barotropic ocean response to moving tropical cyclones: 2. model and simulations. *Journal of Geophysical Research: Oceans*, **124 (5)**, 3462–3485.

Kudryavtsev, V., M. Yurovskaya, and B. Chapron, 2021: Self-similarity of surface wave developments under tropical cyclones. *Journal of Geophysical Research: Oceans*, **126 (4)**, e2020JC016 916.

Landsea, C. W., and J. L. Franklin, 2013: Atlantic hurricane database uncertainty and presentation of a new database format. *Monthly Weather Review*, **141 (10)**, 3576–3592.

Manaster, A., L. Ricciardulli, and T. Meissner, 2021: Tropical cyclone winds from windsat, amsr2, and smap: Comparison with the hwrf model. *Remote Sensing*, **13 (12)**, 2347.

826 Meissner, T., L. Ricciardulli, and A. Manaster, 2021: Tropical cyclone wind speeds from windsat,
827 amsr and smap: Algorithm development and testing. *Remote Sensing*, **13 (9)**, 1641.

828 Meissner, T., L. Ricciardulli, and F. J. Wentz, 2017: Capability of the smap mission to measure
829 ocean surface winds in storms. *Bulletin of the American Meteorological Society*, **98 (8)**, 1660–
830 1677.

831 Mouche, A., B. Chapron, J. Knaff, Y. Zhao, B. Zhang, and C. Combot, 2019: Copolarized
832 and cross-polarized sar measurements for high-resolution description of major hurricane wind
833 structures: Application to irma category 5 hurricane. *Journal of Geophysical Research: Oceans*,
834 **124 (6)**, 3905–3922.

835 Mouche, A. A., B. Chapron, B. Zhang, and R. Husson, 2017: Combined co-and cross-polarized sar
836 measurements under extreme wind conditions. *IEEE Transactions on Geoscience and Remote*
837 *Sensing*, **55 (12)**, 6746–6755.

838 Mueller, K. J., M. DeMaria, J. Knaff, J. P. Kossin, and T. H. Vonder Haar, 2006: Objective esti-
839 mation of tropical cyclone wind structure from infrared satellite data. *Weather and forecasting*,
840 **21 (6)**, 990–1005.

841 Polverari, F., M. Portabella, W. Lin, J. W. Sapp, A. Stoffelen, Z. Jelenak, and P. S. Chang, 2021: On
842 high and extreme wind calibration using ascat. *IEEE Transactions on Geoscience and Remote*
843 *Sensing*, **60**, 1–10.

844 Portabella, M., A. S. Rabaneda, and G. Grieco, 2022: Maxss: Algorithm theoretical baseline
845 document for sfmr-based satellite-derived extreme wind recalibration (v2. 0).

846 Powell, M. D., P. J. Vickery, and T. A. Reinhold, 2003: Reduced drag coefficient for high wind
847 speeds in tropical cyclones. *Nature*, **422 (6929)**, 279–283.

848 Price, J. F., 1981: Upper ocean response to a hurricane. *Journal of Physical Oceanography*, **11 (2)**,
849 153–175.

850 Quilfen, Y., B. Chapron, T. Elfouhaily, K. Katsaros, and J. Tournadre, 1998: Observation of
851 tropical cyclones by high-resolution scatterometry. *Journal of Geophysical Research: Oceans*,
852 **103 (C4)**, 7767–7786.

Quilfen, Y., C. Prigent, B. Chapron, A. Mouche, and N. Houti, 2007: The potential of quikscat and windsat observations for the estimation of sea surface wind vector under severe weather conditions. *Journal of Geophysical Research: Oceans*, **112 (C9)**.

Reul, N., and B. Chapron, 2003: A model of sea-foam thickness distribution for passive microwave remote sensing applications. *Journal of Geophysical Research: Oceans*, **108 (C10)**.

Reul, N., B. Chapron, E. Zabolotskikh, C. Donlon, Y. Quilfen, S. Guimbard, and J.-F. Piolle, 2016: A revised l-band radio-brightness sensitivity to extreme winds under tropical cyclones: The five year smos-storm database. *Remote Sensing of Environment*, **180**, 274–291.

Reul, N., J. Tenerelli, B. Chapron, D. Vandemark, Y. Quilfen, and Y. Kerr, 2012: Smos satellite l-band radiometer: A new capability for ocean surface remote sensing in hurricanes. *Journal of Geophysical Research: Oceans*, **117 (C2)**.

Reul, N., and Coauthors, 2017: A new generation of tropical cyclone size measurements from space. *Bulletin of the American Meteorological Society*, **98 (11)**, 2367–2385.

Riehl, H., 1963: Some relations between wind and thermal structure of steady state hurricanes. *Journal of Atmospheric Sciences*, **20 (4)**, 276–287.

Sampson, C. R., E. M. Fukada, J. A. Knaff, B. R. Strahl, M. J. Brennan, and T. Marchok, 2017: Tropical cyclone gale wind radii estimates for the western north pacific. *Weather and Forecasting*, **32 (3)**, 1029–1040.

Sapp, J., Z. Jelenak, P. Chang, C. Shoup, and J. Carswell, 2022: Processing of high-resolution hurricane ida boundary layer winds from the iwrap instrument on the noaa wp-3d aircraft. *IGARSS 2022-2022 IEEE International Geoscience and Remote Sensing Symposium*, IEEE, 7286–7289.

Schreck III, C. J., K. R. Knapp, and J. P. Kossin, 2014: The impact of best track discrepancies on global tropical cyclone climatologies using ibtracs. *Monthly Weather Review*, **142 (10)**, 3881–3899.

Shapiro, L. J., 1983: The asymmetric boundary layer flow under a translating hurricane. *Journal of Atmospheric Sciences*, **40 (8)**, 1984–1998.

Soisuvarn, S., Z. Jelenak, P. S. Chang, S. O. Alsweiss, and Q. Zhu, 2012: Cmod5. h—a high wind geophysical model function for c-band vertically polarized satellite scatterometer measurements. *IEEE Transactions on Geoscience and Remote Sensing*, **51 (6)**, 3744–3760.

Stoffelen, A., J. A. Verspeek, J. Vogelzang, and A. Verhoef, 2017: The cmod7 geophysical model function for ascat and ers wind retrievals. *IEEE Journal of Selected Topics in Applied Earth Observations and Remote Sensing*, **10 (5)**, 2123–2134.

Takagi, H., and W. Wu, 2016: Maximum wind radius estimated by the 50 kt radius: improvement of storm surge forecasting over the western north pacific. *Natural Hazards and Earth System Sciences*, **16 (3)**, 705–717.

Tsukada, T., and T. Horinouchi, 2023: Strong relationship between eye radius and radius of maximum wind of tropical cyclones. *Monthly Weather Review*, **151 (2)**, 569–588.

Uhlhorn, E. W., P. G. Black, J. L. Franklin, M. Goodberlet, J. Carswell, and A. S. Goldstein, 2007: Hurricane surface wind measurements from an operational stepped frequency microwave radiometer. *Monthly Weather Review*, **135 (9)**, 3070–3085.

Vickery, P. J., and D. Wadhera, 2008: Statistical models of holland pressure profile parameter and radius to maximum winds of hurricanes from flight-level pressure and h* wind data. *Journal of Applied Meteorology and climatology*, **47 (10)**, 2497–2517.

Vinour, L., S. Jullien, A. Mouche, C. Combot, and M. Mangeas, 2021: Observations of tropical cyclone inner-core fine-scale structure, and its link to intensity variations. *Journal of the Atmospheric Sciences*, **78 (11)**, 3651–3671.

Wang, S., and R. Toumi, 2021: Recent tropical cyclone changes inferred from ocean surface temperature cold wakes. *Scientific Reports*, **11 (1)**, 22 269.

Willoughby, H., and M. Rahn, 2004: Parametric representation of the primary hurricane vortex. part i: Observations and evaluation of the holland (1980) model. *Monthly Weather Review*, **132 (12)**, 3033–3048.

Willoughby, H. E., R. Darling, and M. Rahn, 2006: Parametric representation of the primary hurricane vortex. part ii: A new family of sectionally continuous profiles. *Monthly weather review*, **134 (4)**, 1102–1120.

Wright, C. W., and Coauthors, 2001: Hurricane directional wave spectrum spatial variation in the open ocean. *Journal of Physical Oceanography*, **31 (8)**, 2472–2488.

Young, I. R., 2017: A review of parametric descriptions of tropical cyclone wind-wave generation. *Atmosphere*, **8 (10)**, 194.

Yueh, S. H., A. G. Fore, W. Tang, A. Hayashi, B. Stiles, N. Reul, Y. Weng, and F. Zhang, 2016: Smap l-band passive microwave observations of ocean surface wind during severe storms. *IEEE Transactions on Geoscience and Remote Sensing*, **54 (12)**, 7339–7350.

Zabolotskikh, E. V., L. M. Mitnik, N. Reul, and B. Chapron, 2015: New possibilities for geophysical parameter retrievals opened by gcom-w1 amsr2. *IEEE journal of selected topics in applied earth observations and remote sensing*, **8 (9)**, 4248–4261.

Zhao, Y., A. A. Mouche, B. Chapron, and N. Reul, 2018: Direct comparison between active c-band radar and passive l-band radiometer measurements: Extreme event cases. *IEEE Geoscience and Remote Sensing Letters*, **15 (6)**, 897–901.